Characterization of rockfalls from seismic signal: insights from laboratory experiments

Maxime Farin, Anne Mangeney, Renaud Toussaint, Julien de Rosny, Nikolai Shapiro, Thomas Dewez, Clément Hibert, Christian Mathon, Olivier Sedan, Frédéric Berger

Characterization of rockfalls from seismic signal: insights from laboratory experiments

Maxime Farin,[1] Anne Mangeney,[1,2], Renaud Toussaint,[3], Julien de Rosny[4], Nikolai Shapiro[1], Thomas Dewez[5], Clément Hibert[6], Christian Mathon[5], Olivier Sedan[5], and Frédéric Berger[7]

.

Corresponding author: Maxime Farin, Seismology team, Institut de Physique du Globe de Paris, 1 rue Jussieu, 75238 Paris cedex 05, France. (farin@ipgp.fr)

[1]Institut de Physique du Globe de Paris, Sorbonne Paris Cité, CNRS (UMR 7154), Paris, France

[2]ANGE team, CEREMA, Inria, Lab. J.-L. Lions, CNRS, Paris, France

[3]IPGS-EOST, Géophysique Expérimentale, CNRS, Strasbourg, France

[4]Institut Langevin, Laboratoire Ondes et Acoustique, CNRS, Paris, France

[5]Service des Risques Naturels, BRGM, Orléans la Source, France

Abstract. The seismic signals generated by rockfalls can provide information on their dynamics and location. However, the lack of field observations makes it difficult to establish clear relationships between the characteristics of the signal and the source. In this study, scaling laws are derived from analytical impact models to relate the mass and the speed of an individual impactor to the radiated elastic energy and the frequency content of the emitted seismic signal. It appears that the radiated elastic energy and frequencies decrease when the impact is viscoelastic or elasto-plastic compared to the case of an elastic impact. The scaling laws are validated with laboratory experiments of impacts of beads and gravels on smooth thin plates and rough thick blocks. Regardless of the involved materials, the masses and speeds of the impactors are retrieved from seismic measurements within a factor of 3. A quantitative energy budget of the impacts is established. On smooth thin plates, the lost energy is either radiated in elastic waves or dissipated in viscoelasticity when the impactor is large or small with respect to the plate thickness, respectively. In contrast, on rough thick blocks, the elastic energy radiation represents less than 5% of the lost energy. Most of

[6]Lamont-Doherty Earth Observatory,

Palisades NY, US

[7]Unité de Recherche Ecosystèmes

Montagnards, Cemagref, Grenoble, France

the energy is lost in plastic deformation or rotation modes of the bead owing to surface roughness. Finally, we estimate the elastic energy radiated during field scale rockfalls experiments. This energy is shown to be proportional to the boulder mass, in agreement with the theoretical scaling laws.

1. Introduction

Rockfalls represent a major natural hazard in steep landscapes. Because of their unpredictable and spontaneous nature, the seismic monitoring of these gravitational instabilities has raised a growing interest for risks assessment in the last decades. Recent studies showed that rockfalls can be automatically detected and localized with high precision from the seismic signal they generate [*Suriñach et al.*, 2005; *Deparis et al.*, 2008; *Dammeier et al.*, 2011; *Hibert et al.*, 2011, 2014a]. A burning challenge is to obtain quantitative information on the gravitational event (volume, propagation velocity, extension,...) from the characteristics of the associated seismic signal [*Norris*, 1994; *Deparis et al.*, 2008; *Vilajosana et al.*, 2008; *Favreau et al.*, 2010; *Dammeier et al.*, 2011; *Hibert et al.*, 2011, 2014a; *Moretti et al.*, 2012, 2015; *Yamada et al.*, 2012].

Some authors found empirical relationships between the rockfall volume and the maximum amplitude of the signal or the radiated seismic energy [*Norris*, 1994; *Hibert et al.*, 2011; *Yamada et al.*, 2012]. The precursory work of *Norris* [1994] on rockfalls of large volume $> 10^4$ m^3 at Mount St Helens showed that the maximum amplitude of the emitted signal depends linearly on the rockfall volume. This is in agreement with the observations of *Yamada et al.* [2012] on landslides triggered in Japan by Typhoon Talas in 2011. The authors observed that the integral of the squared signal amplitude measured at 1 km from the source varied as the square the landslide volume. In contrast, *Hibert et al.* [2011] showed that the seismic energy emitted by rockfalls is proportional to their volume in the Dolomieu crater of the Piton de la Fournaise volcano, Réunion Island. Moreover, *Dammeier et al.* [2011] used a statistical approach and estimated the volume V of several

rockfalls in the central Alps from the measurement of the duration t_s, enveloppe area EA and peak amplitude PA of the generated seismic signal. For twenty well constrained events, they found the empirical scaling law: $V \propto t_s^{1.0368} EA^{-0.1248} PA^{1.1446}$. The volumes estimated with this relation were close to the measured ones but the results were sensitive to the distance of the seismic stations from the events.

Other surveys investigated the ratio of the radiated seismic energy W_{el} over the potential energy ΔE_p lost by the rockfalls from initiation to deposition [*Deparis et al.*, 2008; *Hibert et al.*, 2011, 2014a; *Lévy et al.*, 2015]. *Deparis et al.* [2008] studied ten rockfalls that occurred between 1992 and 2001 in the french Alps and estimated that the ratio $W_{el}/\Delta E_p$ was between 10^{-5} and 10^{-3}. *Hibert et al.* [2011, 2014a] observed that the ratios of the seismic energy W_{el} radiated by the rockfalls in the Dolomieu crater over their potential energy lost ΔE_p varied from 5.10^{-5} to 2.10^{-3}. Finally, *Lévy et al.* [2015] found $W_{el}/\Delta E_p \approx 1.1.10^{-5} - 2.8.10^{-5}$ for pyroclastic and debris flows that occurred on the Souffrière Hills volcano in Montserrat Island, Lesser Antilles. Most of the aforementioned studies focused on a specific rockfalls site [*Norris*, 1994; *Deparis et al.*, 2008; *Dammeier et al.*, 2011; *Hibert et al.*, 2011, 2014a; *Yamada et al.*, 2012; *Lévy et al.*, 2015]. It is however difficult to test the developed techniques on other sites because only a few of rockfalls areas are nowadays simultaneously seismically and optically monitored.

Because gravitational events are very complex, it is still not clear what parameters controls their seismic emission. The seismic signals generated by rockfalls on the field are partially composed of waves emitted by individual impacts of boulders, triggering high frequencies noise, typically higher than 1 Hz [e.g. *Deparis et al.*, 2008; *Vilajosana et al.*, 2008; *Helmstetter and Garambois*, 2010; *Hibert et al.*, 2014b; *Lévy et al.*, 2015] and by

long period stresses variations owing to the mass acceleration and deceleration over the topography, responsible for lower frequencies in the signal (< 1 Hz) [e.g. *Kanamori and Given*, 1982; *Favreau et al.*, 2010; *Allstadt*, 2013]. To start the work on understanding the seismic emission of rockfalls, we focus here on the seismic signal generated by impacts.

The dynamics of impact can be described at first order by the classical model proposed by *Hertz* [1882] that gives the analytical expression of the force of impact of an elastic sphere on a solid elastic surface [see *Johnson*, 1985]. From the comparison of the impacts forces and durations measured from the emitted seismic signal with that predicted by *Hertz* [1882], *Buttle and Scruby* [1990] and *Buttle et al.* [1991] managed to retrieve the diameter of sub-millimetrical particles impacting a thick block. However, their computation was based on the direct compressive wave, measured at the opposite of the impact on the target block. Their configuration can therefore not be exported to field context. Also based on *Hertz* [1882]'s theory, *Tsai et al.* [2012] expressed the long period power spectral density generated by the impacts of sediments on the bed of rivers as a function of the river parameters such the particle size distribution, the impact rate and the bed load flux. From seismic measurements of *Burtin et al.* [2008] on trans-Himalayan Trisuli River, *Tsai et al.* [2012] were then able to quantitatively deduce the bed load flux.

In this paper, we adopt a similar approach. The basic idea is to derive from *Hertz* [1882]'s model analytical scaling laws relating the radiated elastic energy and the frequencies of the seismic signal generated by an impact to the mass and the speed of the impactor. These laws can then be inverted to deduce the impact parameters from a measurement of the emitted seismic signal. Note that *Tsai et al.* [2012] assumed for their analytical model that the impact duration was instantaneous because they focused on

signals of long periods compared with this duration. On the contrary, we do not assume an instantaneous impact here because we try here to use the whole spectrum content. Indeed, in order to robustly estimate the impact parameters from the emitted signal using our scaling laws, we need to determine the absolute energy radiated in elastic waves and, therefore, the entire amplitude spectrum of the seismic signal generated by the impact. This implies:

1. to record signal periods much smaller than the impact duration;

2. to know well the elastic properties of the impactor and of the substrate, i.e. their elastic modulii, their density, the type of mode excited in the substrate after an impact, its dispersion and how its energy attenuates with increasing distance from the source.

These two conditions are not easy to address in the field because usual sampling times are of the order of the typical impact durations ($\sim$ 0.01 s) and because of the strong heterogeneity of the ground. Therefore, in order to test our analytical scaling laws, we perform controlled laboratory experiments of impacts of spherical beads on thin plates with an ideal smooth surface, then on rough thick blocks i.e., in a context similar to that of the field. A series of impact experiments is also conducted with gravels to quantify how the relations between impacts properties and signal characteristics change when the impactor has a rough surface, which is a more realistic case i.e., closer to what is observed for natural rockfalls.

During an impact, a significant part of the impactor's energy can be lost in inelastic processes such as plastic i.e., irreversible, deformation of the impactor or the ground [*Davies*, 1949] or viscoelastic dissipation in the vicinity of the impact [*Falcon et al.*, 1998]. These losses are not considered in *Hertz* [1882]'s elastic impact model. In this paper, we use

analytical models of viscoelastic and elasto-plastic impact to estimate how the frequencies of the emitted vibration and the radiated elastic energy deviate from that predicted using *Hertz* [1882]'s theory when inelastic dissipation occurs. Using these models, we interpret the discrepancy observed between the measured values in our experiments and those predicted by the elastic model of *Hertz* [1882]. Another advantage of the laboratory experiments is that the total energy lost during the impact can be easily measured from the velocity change of the impactor before and after the impact. We can then establish a quantitative energy budget among the energy radiated in elastic waves and that dissipated in inelastic processes. This allow us to better understand the process of wave generation by an impact and to roughly extrapolate what should be the relative importance of the different loss processes for natural rockfalls.

This paper is structured as follows. In section 2, we recall the theory for elastic, viscoelastic and elasto-plastic impacts of a sphere on a plane surface and we derive the analytical scaling laws from this theory. The experimental setup is presented in section 3. In section 4, we test experimentally the scaling laws established in section 2 and retrieve the masses and speeds of the impactors from the measured seismic signals. In addition, we establish the energy budget of the impacts among elastic and inelastic losses and observe how this budget varies on smooth thin plates and rough thick blocks when the bead mass and the elastic parameters change. In section 5, the discrepancy of the experimental results with the theory is discussed. Finally, the analytical scaling laws demonstrated in this paper are compared with empirical relations observed in drop experiments of large boulders in a natural context. We identify the issues that should be overcome in order to apply our scaling laws to natural impact situations.

2. Theory: Relations Between Impact Parameters and Seismic Characteristics

The vibration displacement $\mathbf{u}(\mathbf{r},t)$ at the distance $\mathbf{r}$ from an impact is given by the time convolution of the force $\mathbf{F}(\mathbf{r}_s,t)$ applied to the ground at position r_s with the Green's function $\bar{\bar{\mathbf{G}}}(\mathbf{r},\mathbf{r}_s,t)$ of the structure where the wave propagates [*Aki and Richards*, 1980]:

$$\mathbf{u}(\mathbf{r},t) = \bar{\bar{\mathbf{G}}}(\mathbf{r},\mathbf{r}_s,t) * \mathbf{F}(\mathbf{r}_s,t), \tag{1}$$

where $*$ stands for the time convolution product. In our experiments, we only have access to the vibration acceleration in the direction normal to the surface $a_z(r,t)$. In the time Fourier domain, this acceleration is given by:

$$\tilde{A}_z(r,f) = -(2\pi f)^2 \tilde{G}_{zz}(r,f)\tilde{F}_z(f), \tag{2}$$

where f is the frequency and $\tilde{F}_z(f)$ is the time Fourier transform of the vertical impact force $F_z(t)$. The expression of the Green's function $\tilde{G}_{zz}(r,f)$ is different when the impact duration is greater or smaller than the two-way travel time of the emitted wave in the structure thickness, i.e. for impacts on thin plates and on thick blocks, respectively. A plate of thickness h vibrates normally to its surface because the fundamental A_0 mode of Lamb carries most of the energy [*Royer and Dieulesaint*, 2000; *Farin et al.*, 2015]. The module of the Green's function of this mode of vibration can be approximated by [e.g. *Goyder and White*, 1980]:

$$|\tilde{G}_{zz}(r,f)| = \frac{1}{8Bk^2}\sqrt{\frac{2}{\pi kr}}, \tag{3}$$

where k is the wave number, $B = h^3E_p/12(1-\nu_p^2)$ is the bending stiffness and E_p and ν_p are the Young's modulus and the Poisson ratio of the impacted structure, respectively. At low frequencies i.e., for $kh << 1$, the wave number k is related to the angular frequency ω by $k^4 = \omega^2\rho_p h/B$, where ρ_p is the plate density.

In contrast, an impact on a thick block generates compressive, shear and Rayleigh waves [*Miller and Pursey*, 1955; *Aki and Richards*, 1980]. For $kr >> 1$ i.e., in far field, the displacement mainly results from Rayleigh waves and the Green's function can be approximated by [*Miller and Pursey*, 1955; *Farin et al.*, 2015]:

$$|\tilde{G}_{zz}(r,f)| \approx \frac{\xi^2\omega}{2\mu c_P}\frac{\sqrt{x_0(x_0^2-1)}}{f_0'(x_0)}\sqrt{\frac{2c_P}{\pi\omega r}}, \tag{4}$$

where μ is the shear Lamé coefficient, c_P is the compressional wave speed, $\xi = \sqrt{2(1-\nu_p)/(1-2\nu_p)}$, $f_0(x) = (2x^2-\xi^2)^2 - 4x^2\sqrt{(x^2-1)(x^2-\xi^2)}$ and x_0 is the real root of f_0.

In this section, we derive analytical scaling laws that relate the energy radiated in elastic waves and the characteristic frequencies of the vibration $\tilde{A}_z(r,f)$ emitted by an impact to the impact parameters (mass m, speed V_z). Because the vibration $\tilde{A}_z(r,f)$ is controlled by the impact force $\tilde{F}_z(f)$ [equation (2)], the scaling laws are different when the impact is elastic or when viscoelastic dissipation or plastic deformation occur. Let us first recall the expression of the impact force for an elastic impact and how it changes for an inelastic impact. Note that we do not use any elasto-visco-plastic model of impact here because elastic energy radiation, viscoelastic dissipation and plastic deformation are never simultaneously significant in our experiments, even though it could be the case on the field. For example, in certain cases, viscoelastic and plastic losses are negligible and an elastic impact model is sufficient to describe the energy transfer.

2.1. Impact Models

2.1.1. Elastic Impact Model

2.1.1.1. Hertz's Model

148 *Hertz* [1882] gives the force of elastic contact of a sphere of mass m on a plane as a
149 function of their interpenetration depth $\delta_z(t)$ (Figure 1a):

$$F_z(t) = -K\delta_z^{3/2}(t), \tag{5}$$

151 where

$$K = \frac{4}{3}R^{1/2}E^*, \tag{6}$$

153 with R, the sphere radius and $1/E^* = (1-\nu_s^2)/E_s + (1-\nu_p^2)/E_p$, where ν_s, ν_p, E_s, E_p are
154 respectively the Poisson's ratios and the Young's moduli of the constitutive materials of
155 the sphere and the impacted plane.

156 During an impact, the displacement of the center of mass of the sphere is equal to the
157 interpenetration $\delta_z(t)$. Neglecting the gravity force, the equation of motion of the sphere
158 is then:

$$m\frac{\mathrm{d}^2\delta_z(t)}{\mathrm{d}t^2} = -K\delta_z^{3/2}(t). \tag{7}$$

160 The solution of equation (7) is of the form $\delta_z(t) = \delta_{z0}f(t/T_c)$. The maximum interpene-
161 tration depth δ_{z0} and the impact duration T_c are respectively given by [*Johnson*, 1985]:

$$\delta_{z0} = \left(\frac{5mV_z^2}{4K}\right)^{2/5}, \tag{8}$$

163 and

$$T_c \approx 2.94\frac{\delta_{z0}}{V_z} \approx 2.87\left(\frac{16m^2}{9K^2V_z}\right)^{1/5}, \tag{9}$$

165 where V_z is the impact speed.

166 The maximum value of the impact force is therefore, according to equation (5):

$$F_0 = K\delta_{z0}^{3/2} = K\left(\frac{5mV_z^2}{4K}\right)^{3/5}, \tag{10}$$

In the following, the interpenetration depth $\delta_z(t)$, the time t and the force $F_z(t)$ are respectively scaled by δ_{z0}, δ_{z0}/V_z and F_0, that contain all the informations on the impact characteristics.

2.1.1.2. Hertz-Zener's model for impacts on thin plates

Hertz [1882]'s model [equation (8)] is valid provided that the energy radiated in elastic waves during the impact represents a small proportion of the impact energy $\frac{1}{2}mV_z{}^{1/2}$ [*Hunter*, 1957; *Johnson*, 1985]. This is not the case when the thickness of the impacted structure is around or lower than the diameter of the impactor, i.e. for impacts on thin plates and membranes [e.g. *Zener*, 1941; *Farin et al.*, 2015]. When the energy lost in plate vibration during the impact is not negligible, *Zener* [1941] proposed a more exact description than *Hertz* [1882]'s model of the interaction between the sphere and the plate's surface. One has to distinguish the sphere displacement z, given by:

$$m\frac{\mathrm{d}^2 z(t)}{\mathrm{d}t^2} = -F_z(t), \tag{11}$$

from the plate's surface displacement u_z at the position of the impact, whose time derivative is:

$$\frac{\mathrm{d}u_z(t)}{\mathrm{d}t} = Y_{el}F_z(t), \tag{12}$$

where Y_{el} is the real part of the time derivative of the Green's function at the impact position $\Re\left(\mathrm{d}G_{zz}(r_0,t)/\mathrm{d}t\right)$, i.e. the radiation admittance. This function is given by [*Goyder and White*, 1980] for plates:

$$Y_{el} = \frac{1}{8\sqrt{B\rho_p h}}, \tag{13}$$

with B, the bending stiffness and h, the plate thickness. In these equations, the impact force $F_z(t)$ follows *Hertz* [1882]'s theory [equation (5)].

The difference of equation (11) and the derivative of equation (12) gives the following equation for the relative movement of the sphere and of the substrate i.e., the interpenetration $\delta_z(t) = z(t) - u_z(t)$, in dimensionless form with $\delta^* = \delta_z/\delta_{z0}$ and $t^* = V_z t/\delta_{z0}$:

$$\frac{\mathrm{d}^2\delta^*}{\mathrm{d}t^{*2}} = -\frac{5}{4}\left(\delta^{*3/2} + \lambda_Z \frac{\mathrm{d}\delta^*}{\mathrm{d}t^*}\delta^{*1/2}\right), \tag{14}$$

with

$$\lambda_Z \approx 0.175 \frac{E^{*2/5}}{\rho_s^{1/15}\sqrt{B\rho_p h}} m^{2/3} V_z^{1/5}. \tag{15}$$

In equation (14), we retrieve the impact model of *Hertz* [1882] [equation (7)] with a corrective term that depends on the parameter λ_Z. This corrective term becomes negligible when the thickness h of the structure is much larger than the diameter d of the impactor because the parameter λ_Z tends towards 0 [*Zener*, 1941]. Therefore, for impacts on elastic half-spaces i.e., on thick blocks, the corrective term disappears and the model of *Zener* [1941] [equation (14)] matches with that of *Hertz* [1882] [equation (7)]. As a consequence, this model is only relevant for impacts on thin plates.

Equation (14) is solved numerically for different values of λ_Z with the initial conditions $\delta^*(0) = 0$ and $\frac{\mathrm{d}\delta^*}{\mathrm{d}t^*}(0) = 1$. The impact force $F_z(t)/F_0 = \delta^{*3/2}$ is shown on Figure 1b. When λ_Z increases i.e., when m and V_z increase, the force profile looses its symmetry with respect to its maximum, its amplitude decreases and its duration increases. For an inelastic coefficient $\lambda_Z = 0.25$, the force is only slightly affected. Practically, λ_Z is always smaller than 0.5 in our experiments.

2.1.2. Viscoelastic Impact Model

Viscoelastic dissipation is related to the viscosities of the materials involved in the impact and can be described as a heat loss. Viscoelastic solids are often represented by

a spring and a dashpot in parallel (Kelvin-Voigt model). *Hertz* [1882]'s theory has been extended to viscoelastic impacts, adding a force $F_{diss}(t)$ in equation (7) to model viscous dissipation [*Kuwabara and Kono*, 1987; *Falcon et al.*, 1998; *Ramírez et al.*, 1999]:

$$F_{diss}(t) = -\frac{3}{2} DK \frac{\mathrm{d}\delta_z(t)}{\mathrm{d}t} \delta_z^{1/2}(t), \tag{16}$$

with D, a characteristic time depending on the materials viscosities and elastic constants [*Hertzsch et al.*, 1995; *Brilliantov et al.*, 1996; *Ramírez et al.*, 1999]. The expression of D is only given in the literature in case when the sphere and the plane have the same elastic parameters E and ν:

$$D = \frac{2}{3} \frac{\chi^2}{(\chi + 2\eta)} \frac{(1-\nu^2)(1-2\nu)}{E\nu^2}, \tag{17}$$

where χ and η are the bulk and shear viscosities, respectively. We can not measure these two last parameters in our experiments and they are not tabulated in our frequencies range of interest, therefore D will be an adjustable parameter.

The dimensionless equation of motion for a viscoelastic impact is then:

$$\frac{\mathrm{d}^2\delta^*}{\mathrm{d}t^{*2}} = -\frac{5}{4} \left(\delta^{*3/2} + \alpha \frac{\mathrm{d}\delta^*}{\mathrm{d}t^*} \delta^{*1/2} \right), \tag{18}$$

which is the same expression as for *Zener* [1941]'s model [equation (14)] but with a different parameter:

$$\alpha = \frac{3}{2} D \frac{V_z}{\delta_{z0}} \simeq 1.4 D \frac{E^{*2/5}}{\rho_s^{1/15}} \frac{V_z^{1/5}}{m^{1/3}}, \tag{19}$$

the viscoelastic parameter [*Ramírez et al.*, 1999]. For $\alpha = 0$ (i.e., $D = 0$), equation (18) matches with equation (7) for elastic impacts.

Because equations (14) and (18) are identical, when α increases the force profile varies exactly the same way as when λ_Z increases in *Zener* [1941]'s model (Figure 1b). However,

233 note that the corrective terms to *Hertz* [1882]'s model in the viscoelastic and *Zener* [1941]'s
234 models have a different physical origin. The viscoelastic corrective term is due to the fact
235 that the impactor and the ground have an intrinsic viscosity [*Falcon et al.*, 1998]. This
236 term is stronger when the mass m, or diameter d, of the sphere decreases [equation (19)].
237 On the contrary, the corrective term of *Zener* [1941]'s model comes from the fact that a
238 larger amount of the impactor's kinetic energy is transferred into plate vibration during
239 the impact when the sphere's diameter d is large compared to the plate thickness h [*Zener*,
240 1941] [equation (15)]. We can therefore assume that the viscoelastic and *Zener* [1941]'s
241 impact models are never simultaneously effective.

242 **2.1.3. Elasto-plastic Impact Model**

243 Plastic (i.e. not reversible) deformations result from irreversible structural modifications
244 which occur when the pressure on the contact area $P(t) = F_z(t)/2\pi R\delta_z(t)$ reaches the
245 dynamic yield strength $P_Y = 3Y_d$ of the material, where Y_d is the dynamic yield stress of
246 the softest material [*Crook*, 1952; *Johnson*, 1985]. Plastic deformation can be evidenced
247 by the apparition of a crater at the impact position. The energy lost to create this crater
248 modifies the shape of the impact force with respect to the case of an elastic or viscoelastic
249 impact. A model was proposed by *Troccaz et al.* [2000] to describe the evolution of the
250 impact force when the limit of elastic behavior is exceeded. This model is based on the
251 hypothesis that only the sphere or the structure deforms plastically. Such an impact is
252 composed of three successive phases:

253 1. The impact is elastic while $P(t) < P_Y$ and the impact force $F(t)$ follows equation
254 (5);

255 2. When $P(t) \geq P_Y$ the deformation is fully plastic and the force expression becomes
256 $F_z(t) = -2\pi R P_Y \delta_z(t)$ until the force reaches a maximum F_{max}, which is smaller than the
257 maximum value F_0 for an elastic impact;

258 3. The rebound is elastic with $F_z(t) = F_{max}\left((\delta_z(t) - \delta_r)/(\delta_{max} - \delta_r)\right)^{3/2}$, where δ_{max}
259 is the maximum interpenetration reached and δ_r is the residual deformation after plastic
260 deformation, that is neglected (i.e., considered to be 0) in the following.

261 The dimensionless equation of motion during plastic deformation (phase 2) is then, if
262 $\delta_z(t)$ and time t are respectively scaled by δ_{z0} and δ_{z0}/V_z:

263
$$\frac{\mathrm{d}^2\delta^*}{\mathrm{d}t^{*2}} = -\frac{5}{4}\frac{P_Y}{P_0}\delta^*, \tag{20}$$

264 where P_0 is the maximum stress during Hertz's elastic impact:

265
$$P_0 = \frac{K\delta_{z0}^{3/2}}{2\pi R\delta_{z0}} = \frac{2}{3\pi}\left(\frac{5}{4}\right)^{1/5}\rho_s^{1/5}E^{*4/5}V_z^{2/5}. \tag{21}$$

266 Equation (20) depends only on the stresses ratio P_Y/P_0 that is independent of the
267 impactor mass m. When this ratio is greater or equal to 1, the impact is purely elastic.
268 The amplitude of the impact force decreases as the stresses ratio P_Y/P_0 decreases (Figure
269 1c). Both the duration of the impact and the time to reach the maximum amplitude
270 increase for an elasto-plastic impact with respect to the elastic case.

2.2. Analytical Scaling Laws

271 The seismic signal generated by an impact can be characterized by the radiated elastic
272 energy W_{el} and by a frequency. Here we relate analytically these seismic characteristics
273 with the mass m and the speed V_z of the impactor using the impact models presented
274 above.

275 2.2.1. Radiated Elastic Energy

The energy W_{el} radiated in elastic waves is the work done by the impact force $F_z(t)$ during the impact, i.e.,

$$W_{el} \hat{=} \int_{-\infty}^{+\infty} F_z(t) \frac{\mathrm{d}u_z(t)}{\mathrm{d}t} \mathrm{d}t = \int_{-\infty}^{+\infty} |\tilde{F}_z(f)|^2 \tilde{Y}_{el}(f) \mathrm{d}f, \tag{22}$$

according to Parceval's theorem, where $\frac{\mathrm{d}u_z(t)}{\mathrm{d}t}$ is the vibration speed at the impact position [equation (12)] and $\tilde{Y}_{el}(f)$ is the time Fourier transform of the radiation admittance.

The radiated elastic energy W_{el} is different for impacts on thin plates and on thick blocks because the radiation admittance $\tilde{Y}_{el}(f)$ has a different expression. Developing equation (22), we obtain in Table 1 analytical expressions for the elastic energy W_{el} radiated during an impact on thin plates and thick blocks, as a function of the impact parameters (see Appendix A for details on the calculations). On thin plates,

$$W_{el} = a_1 C_{plate} m^{5/3} V_z^{11/5} \tag{23}$$

and, on thick blocks,

$$W_{el} = a_2 C_{block} m V_z^{13/5}, \tag{24}$$

where coefficients a_1 and a_2 depends only on the elastic parameters (see Table 1). In these expressions, $C_{plate} = \int_{-\infty}^{+\infty} |g(t^*)|^2 \mathrm{d}t^*$ and $C_{block} = \int_0^{+\infty} f^{*2} |\tilde{g}(f^*)|^2 \mathrm{d}f^*$, where $|g(t^*)| = |F_z(t)|/F_0$ with $t^* = V_z t/\delta_{z0}$ and where $\tilde{g}(f^*)$ is the time Fourier transform of $g(t^*)$. For an elastic impact i.e., with $F_z(t)$ given by equation (5), we obtain $C_{plate} \simeq 1.21$ and $C_{block} \simeq 0.02$. The function $g(t^*)$ has a lower amplitude when the impact is inelastic compared to the case of an elastic impact (Figures 1b and 1c). Therefore, both coefficients C_{plate} and C_{block} decrease when the viscoelastic parameter α increases and when the stresses ratio P_Y/P_0 decreases (Figures 2a and 2b). Moreover, on thin plates C_{plate} also decreases when the parameter λ_Z increases (Figure 2a). As a consequence, less energy is radiated in the

form of elastic waves when the impact is inelastic with respect to the case of an elastic impact.

On thick blocks, the radiated elastic energy W_{el} is proportional to the impactor's mass m for a given impact speed V_z [equation (24)]. Moreover, the ratio of W_{el} over the impact energy $E_c = \frac{1}{2}mV_z^2$ varies as $V_z^{3/5}$ and is independent of the sphere mass m, which is in agreement with *Hunter* [1957]'s findings.

It is important to note that the analytical expressions for the radiated elastic energy W_{el} in Table 1 are only controlled by the impact force F_z and by the rheological parameters of the impactor and the substrate in the vicinity of the impact but do not depend on wave dispersion and viscous dissipation during wave propagation within the substrate.

2.2.2. Characteristic Frequencies

The frequency content of the seismic signal emitted by an impact can give information on the impact duration. To describe the amplitude spectrum $|\tilde{A}_z(r,f)|$ of the acceleration vibration, we can either measure:

1. A mean frequency f_{mean} that is less sensitive to the signal to noise ratio than the frequency for which the amplitude spectrum is maximum [*Vinningland et al.*, 2007a, b]:

$$f_{mean} = \frac{\int_0^{+\infty} |\tilde{A}_z(r,f)| f \mathrm{d}f}{\int_0^{+\infty} |\tilde{A}_z(r,f)| \mathrm{d}f}, \tag{25}$$

2. The bandwidth Δf:

$$\Delta f = 2\sqrt{\frac{\int_0^{+\infty} |\tilde{A}_z(r,f)| f^2 \mathrm{d}f}{\int_0^{+\infty} |\tilde{A}_z(r,f)| \mathrm{d}f} - {f_{mean}}^2}. \tag{26}$$

Regardless of the complexity (fracturation, layers, ...) of the substrate where the waves emitted by the impact propagate, it is important to notice that the mean frequency f_{mean} and the bandwidth Δf are always inversely proportional to the duration of the

impact, which is given by the force history at the position of the impact. Here, we normalize these frequencies by *Hertz* [1882]'s impact duration T_c. The coefficients of proportionality between f_{mean}, Δf and $1/T_c$ are estimated for elastic, viscoelastic and elasto-plastic impacts by computing a synthetic spectrum $|\tilde{A}_z(r,f)|$ using equation (2) with the forces represented in Figures 1b and 1c for different values of α and P_Y/P_0. The frequencies for an elastic impact i.e., for $\alpha = 0$ and $P_Y/P_0 = 1$, are given in Table 2. Both frequencies f_{mean} and Δf are smaller when the impact is inelastic compared to the case of an elastic impact (Figure 3). They decrease by $\sim 5\%$ when α increases from 0 to 0.5 and by $\sim 25\%$ when the stresses ratio P_Y/P_0 decreases from 1 to 0.5.

When normalized by T_c, the characteristic frequencies are also affected by wave dispersion and viscous attenuation of energy during propagation i.e. by the Green's function of the structure. These propagation effects are independent of the profile of the impact force, i.e. of the fact that the impact is elastic or inelastic. For the computation of the characteristic frequencies on thick blocks, we used for simplicity the far field approximation of the Green's function of Rayleigh waves [equation (4)]. This approximation is correct for impacts on homogeneous media such that investigated in the laboratory experiments of section 4. In the field, however, the propagation medium is much more complex and other modes with a different dispersion could develop. In this case, the frequencies normalized by T_c shown in Table 2 could change. Active or passive seismic surveys can allow to evaluate locally the Green's function of a specific site. This Green's function can then be used in equations (25) and (26) to estimate how much the normalized frequencies divert from that computed using the Green's function of Rayleigh waves. This is however beyond the scope of the paper. In addition to dispersion, viscous attenuation of energy during prop-

agation can have a significant influence on the measured frequency on the field, especially for high frequencies. [*Gimbert et al.*, 2014] investigated the amplitude spectrum generated by the turbulent flow in rivers and showed that its central frequency can decrease by a factor of 10 when the distance r from the source increases from 5 m to 600 m, for a quality factor $Q = 20$. To quantify the effect of viscous attenuation on frequencies in our impact experiments, we multiply the synthetic spectrum in equations (25) and (26) by the factor $\exp(-\gamma(\omega)r)$, where $1/\gamma(\omega)$ represents the characteristic distance of energy attenuation. In our experiments, the propagation media are homogeneous and we record the seismic signals close to the impacts, from $r = 2$ cm to about $r = 30$ cm. In this range of distances r and for the substrates investigated in section 4, we estimate that the characteristic frequencies f_{mean} decreases and Δf increases by less than 5% when r increases, which is negligible. However, for every practical applications, it is crucial to evaluate wave dispersion and viscous attenuation during propagation and correct the measured seismic signal from these effects before computing its energy W_{el} and its frequencies f_{mean} and Δf. This correction is systematically performed in our experiments.

2.2.3. Inverse Scaling Laws

We can invert the scaling laws derived in this section for the radiated elastic energy W_{el} and for the frequencies f_{mean} and Δf (Tables 1 and 2) to express the mass m and the impact speed V_z as functions of the radiated elastic energy W_{el} and a characteristic frequency f_c of the seismic signal that is either f_{mean} or Δf.

On thin plates, $W_{el} = a_1 C_{plate} m^{5/3} V_z^{11/5}$, $f_{mean} = 0.75/T_c$ and $\Delta f = 0.72/T_c$, then, developing the expression of T_c [equation (9)], we obtain:

$$m = c_1 \left(\frac{E^{*2}}{(a_1 C_{plate})^{3/11} \rho_s^{1/3}} \right)^{11/16} \frac{W_{el}^{3/16}}{f_c^{33/16}} \tag{27}$$

and

$$V_z = c_2 \left(\frac{\rho_s^{1/3}}{a_1 C_{plate} E^{*2}} \right)^{5/16} W_{el}^{5/16} f_c^{25/16}, \tag{28}$$

where $c_1 \approx 0.046$ or 0.05 and $c_2 \approx 10.8$ or 10.1 if f_c is f_{mean} or Δf, respectively. The coefficient a_1 is given in Table 1.

On thick blocks, the inversion of the relations $W_{el} = a_2 C_{block} m V_z^{13/5}$, $f_{mean} = 1/T_c$ and $\Delta f = 0.6/T_c$ gives:

$$m = c_3 \left(\frac{E^{*6/5}}{(a_2 C_{block})^{3/13} \rho_s^{1/5}} \right)^{13/16} \frac{W_{el}^{3/16}}{f_c^{39/16}} \tag{29}$$

and

$$V_z = c_4 \left(\frac{\rho_s^{1/5}}{a_2 C_{block} E^{*6/5}} \right)^{5/16} W_{el}^{5/16} f_c^{15/16}, \tag{30}$$

where $c_3 \approx 4.88$ or 4.7 and $c_4 \approx 0.018$ or 0.02 if f_c is f_{mean} or Δf, respectively. The value of a_2 is given in Table 1.

The physical characteristics of an impact can then be theoretically deduced from the generated seismic signal. With a continuous recording the seismic signals emitted by rockfalls, such that performed in Dolomieu crater, Réunion Island [e.g. *Hibert et al.*, 2014a], the relations (27) to (30) could be very useful for risks assessment related to these events. Note that the estimation of the impact parameters m and V_z requires a prior evaluation of the elastic properties ρ_i, E_i and ν_i of the impactor and the ground. It should also be noticed that m and V_z strongly depend on the frequency f_c. For example

on blocks, if the characteristic frequency is underestimated by a factor of 2, the mass m will be overestimated by a factor of $2^{39/16} \simeq 5.4$. It is therefore necessary to record the entire frequency spectrum to obtain a good estimation of the impact parameters. Because of temporal aliasing during signal sampling, an ideal sampling frequency should be higher than two times the highest frequency of the spectrum, that should be at least $f_{mean} + \Delta f/2$. According to Table 2, the sampling frequency should then be at minimum $3/T_c$.

In section 4.3, the scaling laws presented in Tables 1 and 2 are tested with impacts experiments. Moreover, the masses m and the speeds V_z of the impactors in the experiments are retrieved from the measured seismic signals using equations (27) to (30) and they are compared with their real values.

2.3. Energy Budget and Coefficient of Restitution

Another objective of this paper is to establish an energy budget of the impacts. To that way, we compare the radiated elastic energy W_{el} to the total energy lost during the impact ΔE_c. From a practical point of view, the total energy lost by a spherical bead rebounding normally and without rotation can be easily measured from the difference of the bead kinetic energy before and after the impact:

$$\Delta E_c = \frac{1}{2} m V_z^2 (1 - e^2), \tag{31}$$

where e is the normal coefficient of restitution, that is the ratio of the bead vertical speeds after and before the impact, respectively V' and V_z [e.g. *Tillett*, 1954; *Hunter*, 1957; *Reed*, 1985; *Falcon et al.*, 1998; *McLaskey and Glaser*, 2010].

ΔE_c is the sum of the energy radiated in elastic waves (W_{el}), lost in viscoelastic dissipation in the vicinity of the contact (W_{visc}) and dissipated by all other processes (W_{other}). These other losses can be due to plastic deformation [*Davies*, 1949], surface forces between the sphere and the surface, as e.g. electrostatic forces [*Israelachvili*, 2002], or in general grain scale interactions [*Duran*, 2010; *Andreotti et al.*, 2013]:

$$\Delta E_c = W_{el} + W_{visc} + W_{other}. \tag{32}$$

In our impacts experiments, the radiated elastic energy W_{el} is deduced from a measurement of the generated seismic signal. Here we present an analytical expression for the energy W_{visc} that will be used later to estimate the losses related to viscoelastic dissipation.

2.3.1. Energy Lost by Viscoelastic Dissipation

The energy W_{visc} lost by viscoelastic dissipation in the vicinity of the impact results from the work done by the viscoelastic force $F_{diss} = -\frac{3}{2}DK\frac{\mathrm{d}\delta_z(t)}{\mathrm{d}t}\delta_z^{1/2}(t)$ during the impact:

$$W_{visc} = \int_0^{+\infty} F_{diss}(t).\frac{\mathrm{d}\delta_z(t)}{\mathrm{d}t}\mathrm{d}t. \tag{33}$$

Using the dimensionless variables $\delta^* = \delta_z/\delta_{z0}$ and $t^* = V_z t/\delta_{z0}$ and the viscoelastic parameter $\alpha = \frac{3}{2}DV_z/\delta_{z0}$, we can show that:

$$W_{visc} = C_{visc} m V_z^2, \tag{34}$$

where $C_{visc} = \int_0^{+\infty}\left(\frac{\mathrm{d}\delta^*}{\mathrm{d}t^*}\right)^2\delta^{*1/2}\mathrm{d}t^*$ is a function of α only (Figure 2c). For an elastic impact, no work is done by the viscoelastic force because $C_{visc} = 0$. The expression of W_{visc} is independent of the fact that the impact is on a plate or on a block because it concerns the energy dissipated in the impact region.

The proportion of total energy E_c dissipated by viscoelasticity can be developed in powers of the mass m and the impact speed V_z using the third order Taylor series $C_{visc} \approx 1.24\alpha - 1.51\alpha^2 + 0.86\alpha^3$ and the expression of α in equation (19):

$$\frac{W_{visc}}{E_c} = 2C_{visc} \approx 3.47x - 5.92x^2 + 4.72x^3 + O(x^3), \tag{35}$$

where $x = DE^{*2/5}\rho_s^{-1/15}m^{-1/3}V_z^{1/5}$, which is in agreement with the viscoelastic impact models of *Kuwabara and Kono* [1987] and *Ramírez et al.* [1999].

2.3.2. Total Energy Lost

Finally, if we assume that the sole energy dissipation processes are elastic waves radiation and viscoelastic dissipation and that other energy dissipation processes (e.g. plastic deformation) are negligible, the proportion of the lost energy ΔE_c radiated in elastic waves is, on plates:

$$\frac{W_{el}}{\Delta E_c} = \frac{a_1 C_{plate} m^{2/3} V_z^{1/5}}{a_1 C_{plate} m^{2/3} V_z^{1/5} + C_{visc}}, \tag{36}$$

and the proportion of the lost energy ΔE_c dissipated in viscoelasticity is:

$$\frac{W_{visc}}{\Delta E_c} = \frac{C_{visc}}{a_1 C_{plate} m^{2/3} V_z^{1/5} + C_{visc}}. \tag{37}$$

In these expressions, at first order $C_{visc} \propto m^{-1/3}$ [equation (35)]. Therefore, when the mass m of the impactor increases, the proportion of the lost energy ΔE_c radiated in elastic waves should tends towards 100% and that lost by viscoelastic dissipation should tends toward 0%. The transition from a viscoelastic impact (for small masses) towards an elastic impact (for large masses) occurs when $a_1 C_{plate} m^{2/3} V_z^{1/5} = C_{visc}$, i.e. for a critical mass $m_c \approx 8D\sqrt{B\rho_p h}$.

445 On blocks, we get:

446 $$\frac{W_{el}}{\Delta E_c} = \frac{a_2 C_{block} V_z^{3/5}}{a_2 C_{block} V_z^{3/5} + C_{visc}}, \tag{38}$$

447 and

448 $$\frac{W_{visc}}{\Delta E_c} = \frac{C_{visc}}{a_2 C_{block} V_z^{3/5} + C_{visc}}. \tag{39}$$

449 For large masses m, the ratio $W_{el}/\Delta E_c$ becomes independent of m and tends towards
450 100% because C_{visc} is negligible. When m decreases, the ratio $W_{el}/\Delta E_c$ decreases and the
451 ratio $W_{visc}/\Delta E_c$ increases.

452 This model is somewhat ideal because the energy dissipated by other processes such as
453 plastic deformation are not negligible when the impactor's mass m is large, in particular
454 when the contact surface is rough. As a consequence, the ratio $W_{el}/\Delta E_c$ practically never
455 reaches 100% when m increases (see section 4.4.2).

456 The validity of theoretical scaling laws established in this section for the radiated elastic
457 energy, the frequencies and the lost energy is tested in section 4 with simple impact
458 experiments. Prior to this, the experimental setup is presented in the next section.

3. Experimental Setup

459 We conduct laboratory experiments of beads and gravels impacts on horizontal hard
460 substrates. The generated seismic vibration is recorded on the surface by mono-component
461 piezoelectric charge shock accelerometers (type 8309, *Brüel & Kjaer*). The response of
462 the sensors is flat between 1 Hz and 54 kHz. The impactor is initially held by a screw
463 and dropped without initial velocity and rotation to ensure reproducibility (Figure 4a).
464 The height of fall H varies between 2 cm and 40 cm. The impact speed V_z is calculated
465 assuming a fall without air friction: $V_z = \sqrt{2gH}$, with g the gravitational acceleration.

We drop spherical beads of steel, glass and polyamide (Figure 4b) of diameter d ranging from 1 mm to 20 mm to observe the influence of the mass and of the elastic parameters on the results. We conduct the same experiments with granite gravels of irregular shapes and of similar size and mass than the beads to test if the analytical scaling laws established for spheres impacts are still valid if the impactor is not spherical. The properties of the impactors used in the experiments are shown in Table 3.

Four target substrates are used: (i) a smooth PMMA plate of dimensions $120 \times 100 \times 1$ cm^3, (ii) a circular 1 cm-thick smooth glass plate of radius 40 cm, (iii) a rough marble block of dimensions $20 \times 20 \times 15$ cm^3 and (iv) a rough concrete pillar of dimensions $3 \times 1.5 \times 0.6$ m^3. The seismic vibration is recorded at different distances from the impacts to measure waves group speed $v_g = \partial\omega/\partial k$ and phase speed $v_\phi = \omega/k$ of the direct wave front in these substrates. These characteristics and the elastic parameters of the investigated structures are summarized in Table 4. Note that we assume that the rheological properties E_p, ν_p and ρ_p of the substrates at the position of the impact are the same than that within the substrates, where the waves propagate. This hypothesis is valid for the homogeneous solids investigated here but it may not be correct in the fractured and layered media encountered in the field, whose elastic properties vary with depth. In any cases, it is necessary to determine these properties in order to quantify the radiated elastic energy W_{el} and to deduce thereafter the impact parameters m and V_z from the seismic signal.

4. Experimental Results

4.1. Methods to Estimate the Radiated Elastic Energy

Let us first describe the signals recorded in our experiments of bead impacts on the different substrates and how we compute the radiated elastic energy W_{el} in each case.

A bouncing bead generates a series of short and impulsive acoustic signals (Figures 5a, 5b, 6a and 6b). The bead can rebound more than 50 times on the smooth glass plate while it rebounds only 2 or 3 times on the concrete block owing to surface roughness (Figures 5b and 6a). We estimate the coefficient of normal restitution $e = \sqrt{H'/H}$ from the time of flight Δt between the successive rebounds because the rebound height is given by $H' = g\Delta t^2/8$ [*Falcon et al.*, 1998; *Farin*, 2015]. The total energy lost during an impact is then given by $1 - e^2$ [see equation (31)].

The PMMA and glass plates and the concrete block are sufficiently large to measure most of the first wave arrival before the return of the first reflections off the lateral sides (Figures 5c, 5f and 6e). In these cases, we estimate the radiated elastic energy W_{el} from the energy flux crossing a surface surrounding the impact, as detailed in *Farin et al.* [2015] i.e., for plates:

$$W_{el} = 2rh\rho_p \int_0^{+\infty} v_g(\omega)|\tilde{V}_z(r,\omega)|^2 \exp\left(\gamma(\omega)r\right) \mathrm{d}\omega, \tag{40}$$

and for blocks:

$$W_{el} = 2\rho_p r v_g c_P \pi_R^{surf}(r) \frac{\beta(f_0'(x_0))^2}{2\pi\xi^4(x_0^2-1)} \int_0^{+\infty} |\tilde{V}_z(r,\omega)|^2 \omega^{-1} \exp\left(\gamma(\omega)r\right) \mathrm{d}\omega. \tag{41}$$

In these expressions, v_g is the group speed, $|\tilde{V}_z(r,\omega)|$ is the time Fourier transform of the vertical vibration speed at the surface and $\pi_R^{surf}(r)$ is the percentage of Rayleigh waves in the signal at the surface at distance r from the impact [*Farin et al.*, 2015]. The factor $\exp\left(\gamma(\omega)r\right)$ compensates viscoelastic dissipation with distance. The characteristic distance of energy attenuation $1/\gamma(\omega)$ is estimated experimentally for every substrates (Table 4) [see *Farin et al.*, 2015, for details]. The coefficient β depends only on the Poisson's ratio ν_p (see Figure 17 in Appendix A).

Because the substrates size is limited, wave reflections off the boundaries are recorded by the sensors. Side reflections are strongly attenuated in PMMA which is a more damping material than glass, concrete and marble (Figure 5c). On contrary, the wave is reflected many times in the glass plate and in the two blocks and its averaged amplitude decreases exponentially with time owing to viscous dissipation during wave propagation (Figures 5d, 6c and 6d). An adjustment of an exponential curve on the squared signal, filtered below 2000 Hz, allows us to quantify the characteristic decay time of energy τ in the substrate (Table 4) [see Appendix B of *Farin et al.*, 2015, for details on the experimental procedure]. This situation is referred to as a diffuse field in the literature [e.g. *Weaver*, 1985; *Mayeda and Malagnini*, 2010; *Sánchez-Sesma et al.*, 2011]. In this case, we can estimate the radiated elastic energy W_{el} from the reflected coda. Indeed, in diffuse field approximation, the squared normal vibration speed averaged over several periods decreases exponentially:

$$\overline{v_z(t)^2} = \overline{v_z(t=0)^2} \exp\left(-\frac{t}{\tau}\right), \tag{42}$$

where $t = 0$ is the instant of the impact. Knowing the characteristic time τ, we extrapolate the vibration speed at the instant $t = 0$ and deduce the radiated elastic energy W_{el} from [*Farin et al.*, 2015]:

$$W_{el} \approx \left(1 + \left(\frac{\mathcal{H}}{\mathcal{V}}\right)^2_{\text{diffuse}}\right) \rho_p V \overline{v_z(t=0)^2}, \tag{43}$$

where V is the block volume and $\left(\frac{\mathcal{H}}{\mathcal{V}}\right)_{\text{diffuse}}$ is the ratio of horizontal to vertical amplitude at the surface of the structure in diffuse field approximation. On thin plates, $\left(\frac{\mathcal{H}}{\mathcal{V}}\right)_{\text{diffuse}} \simeq 0$. On a thick block of Poisson's ratio ν_p, *Sánchez-Sesma et al.* [2011] give $\left(\frac{\mathcal{H}}{\mathcal{V}}\right)_{\text{diffuse}} \approx 1.245 + 0.348\nu_p$. Due to statistical assumptions, the diffuse method leads to larger uncertainties on the results compared to that based on the energy flux [*Farin et al.*, 2015]. However,

it is the only method that can be applied when the first arrival can not be distinguished from its side reflections, as for example in the marble block (Figure 6f).

4.2. Comparison with Synthetic Signals

We compare the measured vibration acceleration $a_z(r,t)$ with a synthetic signal which is the time convolution of *Hertz* [1882]'s force of elastic impact (Figure 1b with $\alpha = 0$) with the Green's function [equations (3) and (4)] (Figures 5e to 5h and 6e to 6h).

A good agreement is observed in terms of amplitude and frequencies on the PMMA plate but the agreement is less satisfactory on the other substrates. On glass, only the beginning of the signal is well reproduced by the theory (Figure 5f). A resonance of the accelerometer coupled to the glass plate for 38 kHz could explain why the recorded vibration lasts longer than the synthetic one (Figure 5f). This effect clearly appears on the Fourier transform of the signal with a peak of energy around 38 kHz (Figure 5h). Using a laser Doppler vibrometer that measures the exact surface vibration speed but with a much lower sensitivity than the accelerometers, we determined that the resonance overestimates the vibration energy by a factor of 4. To compensate this effect, we divide the measured radiated elastic energy W_{el} by this factor. On concrete, the synthetic is significantly different than the recorded signal in terms of higher amplitude and frequencies (Figures 6f and 6h). The impact may be not completely normal to the surface owing to the surface roughness, and this could reduce the energy on the normal component, as discussed later in section 5. On marble, the frequencies of the measured signal are close to that of the synthetic one but the amplitude is higher than in theory, probably because side reflections arrive before the end of the first arrival (Figures 6e and 6g). This has no consequence on the estimation of the radiated elastic energy W_{el} for this block because we use the diffuse

553 method [equation (43)]. Note that the peaks of energy for $f > 50$ kHz in the synthetic
554 spectrum on the concrete and marble block are not visible in the recordings, because the
555 accelerometers are not sensitive in this frequency range (see Appendix B).

4.3. Experimental Test of the Analytical Scaling Laws

556 4.3.1. Radiated Elastic Energy

557 Regardless of the bead material, the measured radiated elastic energy W_{el} on the PMMA
558 and glass plates matches well with the theoretical energy W_{el}^{th} predicted in equation (23)
559 for an elastic impact, with $C_{plate} = 1.21$ (Figure 7). For the smallest and the largest
560 beads investigated, however, the data points separate from the theoretical line and the
561 discrepancy can reach a factor of 5. This is clearer for steel beads (Figures 7c and 7g)
562 and for glass beads on the glass plate (Figure 7e).

563 On blocks, the theory predicts that $W_{el}^{th} \propto mV_z^{13/5}$ (equation (24) and Table 1). The
564 experimental data of beads impacts on the concrete and marble blocks follow qualitatively
565 this law (Figure 8). In most of the experiments, however, the measured energy W_{el} is lower
566 than in theory. Moreover, on concrete, the measured radiated elastic energy W_{el} separates
567 from the theoretical trend for the smallest and the largest beads investigated (Figures 8a,
568 8b and 8c). The discrepancy with the theory on Figures 7 and 8 is interpreted in the
569 discussion.

570 Surprisingly, the elastic energy W_{el} radiated by the impacts of granite gravels follows
571 well the scaling law in $m^{5/3}V_z^{11/5}$ on plates (Figures 7d and 7h) and in $mV_z^{13/5}$ on blocks
572 (Figures 8d and 8h). The measured energy W_{el} is however smaller than in theory, by a
573 factor of 2 on plates and up to 10 times smaller on blocks. The experiments with gravels
574 show that Hertz's analytical model of elastic impact, established for spheres, can also

describe at first order the impact dynamics of impactors with a complex shape. As a consequence, we expect that it may also be applied for natural rockfalls.

4.3.2. Characteristics Frequencies

We compute the mean frequency f_{mean} and the bandwidth Δf using equations (25) and (26), respectively (Figure 9). Note that the seismic signals generated by bead impacts in our experiments contain much higher frequencies (1 Hz - 100 kHz) than those recorded for natural rockfalls (1 Hz - 50 Hz) [e.g. *Deparis et al.*, 2008; *Hibert et al.*, 2011]. This is because the bead diameters are in average smaller than the diameter of natural boulders, that could be from a few millimeters to a few meters large. In addition, the sampling frequency is much higher and high frequencies are much less attenuated in our experiments than on the field.

On the glass plate, as the accelerometers are not sensitive to frequencies larger than 50 kHz, the frequencies computed with these sensors saturate to about 40 kHz for the smallest beads i.e., the smallest impact durations T_c (black crosses on Figures 9c and 9d). Therefore, the accelerometers type 8309 are used only for the impacts that generate energy below 50 kHz. For the signals of higher frequencies, we use in parallel piezoelectric ceramics (MICRO-80, *Physical Acoustics Corporation*) sensitive between 100 kHz to 1 MHz. These last sensors can however not be used to quantify the radiated elastic energy W_{el} since they are not very sensitive to frequencies lower than 100 kHz.

Regardless of the bead material, the frequencies of the signals generated by impacts on PMMA, glass and marble collapse well within $\pm 20\%$ with the theoretical scaling laws of Table 2 as a function of the duration of impact T_c (Figures 9a to 9d, 9g and 9h). The agreement is better for the frequency bandwidth Δf than for the mean frequency

598 f_{mean}. The agreement is also very satisfactory for the granite gravels of complex shape,
599 even though the theoretical values of the frequencies were computed using Hertz's impact
600 model for a sphere (see section 2.2.2).

601 In concrete, the wavelength $c_R/f \approx 1$ cm for frequencies around 40 kHz, which is of the
602 order of the size of the heterogeneities. High frequencies $f > 40$ kHz are therefore strongly
603 attenuated during wave propagation in this block. This could explain the discrepancy with
604 the theory for these frequencies on Figure 9e.

605 **4.3.3. Estimating Impact Properties from the Seismic Signal**

606 We use equations (27) to (30) with the coefficients for an elastic impact $C_{plate} = 1.21$
607 and $C_{block} = 0.02$ to retrieve the mass m and the impact speed V_z of the impactors in
608 our experiments. The agreement with the real values is correct, within a factor of 2 for
609 the mass m (Figure 10a) and within a factor of 3 for the impact speed V_z (Figure 10b),
610 both on smooth thin plates and rough thick blocks. For impacts of rough gravels on the
611 two plates, the predicted values are still close to the real ones, with a factor of 1.5, even
612 when inelastic dissipation occurs. The underestimation of m and V_z in certain cases is
613 consistent with the aforementioned discrepancy of the radiated energy W_{el} with theory
614 (Figures 7 and 8).

615 It is therefore possible to have an estimation of the mass m and the impact speed
616 V_z of an impactor on a plate and on a block from the characteristics of the generated
617 seismic signal, with less than an order of magnitude from the real values, using only *Hertz*
618 [1882]'s analytical model of elastic impact. This method only requires to know the elastic
619 parameters of the involved materials.

4.4. Energy Budget of the Impacts

Inelastic losses during an impact can reduce the energy radiated in the form of elastic waves W_{el} compared to that predicted by *Hertz* [1882]'s model (see section 2.2.1). This may explain part of the discrepancy observed between the measured radiated elastic energy W_{el} and its theoretical value W_{el}^{th} on Figures 7 and 8, and consequently between the values of the masses m and speeds V_z inverted from seismic signals and their real values on Figure 10. In order to interpret these discrepancies, we establish in this section an energy budget of the impacts.

For that purpose, we compare on Figures 11 and 13 the measured radiated elastic energy W_{el} (empty symbols) with the total energy lost during the impact ΔE_c, estimated with the coefficient of restitution e (full symbols). The difference $\Delta E_c - W_{el}$ is likely lost in inelastic processes, such as viscoelastic dissipation or plastic deformation. This allows us to establish an energy budget of the impacts (Figures 12 and 14).

Furthermore, we also compare the measured radiated energy W_{el} with the theoretical one – noted W_{el}^{th}, red line on Figures 11 and 13 –, predicted by the scaling law in Table 1 for an elastic impact, with $C_{plate} = 1.21$ and $C_{block} = 0.02$, respectively. Note that on plates, we take into account the dependence of C_{plate} coefficient to λ_Z parameter for large beads (see section 2.1.1.2 and Figure 2a). The corrected theoretical elastic energy on plates is noted $W_{el}^{th'}$ on Figure 11. The discrepancy with theory is discussed in section 5.1.

4.4.1. Energy Budget on Smooth Thin Plates

On smooth thin plates, the energy ΔE_c lost by the bead during an impact is mostly radiated in elastic waves (W_{el}) or dissipated by viscoelasticity during the impact (W_{visc}) (Figures 11 and 12).

More energy is radiated in elastic waves as the bead mass m and the ratio of the bead diameter d on the plate thickness h increase, regardless of the elastic parameters (empty symbols on Figures 11 and 12). For the smallest beads investigated, only 0.1% to 0.3% of the impact energy E_c is radiated in elastic waves. In contrast, the impact energy E_c can be almost entirely converted into elastic waves when the bead diameter d is greater than the plate thickness h (Figure 11c). For large beads, the measured ratio of W_{el}/E_c is close to the theoretical ratio $W_{el}^{th'}/E_c$ (full red line on Figure 11), but diverges as the bead diameter d decreases.

We adjust the viscoelastic parameter D in equation (35) to match the theoretical expression of the lost energy ratio $\Delta E_c/E_c = W_{el}^{th'}/E_c + W_{visc}/E_c$ (thick green line on Figure 11) with the variation of $1-e^2$ (full symbols). The agreement is found to be the best for values of D ranging from 35 ns to 580 ns (Table 5).

The adjustment of D with experimental data allows us to quantify the viscoelastic energy W_{visc} (blue line on Figure 11). More energy is lost by viscoelastic dissipation as the bead mass m and the ratio d/h decrease and this is almost the sole process of energy loss when the bead diameter d is smaller than $0.2h$ (Figure 12). The transition from a viscoelastic impact towards an elastic impact is observed for the critical mass $m_c \approx 8D\sqrt{B\rho_p h}$, as predicted in section 2.3.2 (at the crossing between the red and blue lines on Figure 11). Interestingly, a bouncing bead loses less of its initial energy E_c for masses m close to the critical mass m_c.

For the largest beads of glass and steel, some energy is likely lost in plastic deformation of the softer material involved (Figure 12). As a matter of fact, we observed small indentations on the surface of the plates after the impacts of these beads but not for polyamide beads.

Note that the energy budget is very different for impacts of rough gravels on the same plates. Indeed, the ratio W_{el}/E_c is $3.3\% \pm 1.8\%$ regardless of the gravel mass m. Moreover, about $33\% \pm 17\%$ of the initial energy is lost in translational energy of rebound and $13\% \pm 11\%$ is converted into rotational energy of the gravel. As a matter of fact, half of the gravel's initial energy is in average lost in plastic deformation. (see Appendix C for more details).

4.4.2. Energy Budget on Rough Thick Blocks

On the rough thick blocks, the energy budget is very different than on the smooth plates (Figures 13 and 14). Indeed, a much smaller proportion of energy seem to be lost in elastic waves and in viscoelastic dissipation. The rest is likely dissipated by other processes such as plastic deformation, adhesion or rotational modes of the bead owing to surface roughness.

The measured radiated elastic energy W_{el} represents only from 0.01% to 2% of the impact energy E_c, regardless of the bead mass m (empty symbols on Figure 13). Theory predicts that the ratio W_{el}^{th}/E_c is independent of the mass m (red line). However, the measured ratio W_{el}/E_c slightly increases with bead mass m on concrete and decreases on marble for different reasons explained in the discussion.

Contrary to plates, it is difficult here to determine what proportion of the lost energy ΔE_c is dissipated by viscoelasticity and what proportion is lost in other processes.

However, one remarks that $1-e^2$ increases when the mass m decreases (full symbols on Figure 13). This variation may be due to viscoelastic dissipation which is stronger when the bead mass m decreases [equation (35)]. We make the strong assumption that the percentage of energy lost in other processes W_{other}/E_c is constant and independent of the bead mass m. We then adjust the viscoelastic coefficient D (Table 5) to fit $\Delta E_c/E_c = W_{el}^{th}/E_c + W_{visc}/E_c + W_{other}/E_c$ (thick green line on Figure 13) with the variation of $1-e^2$ (full symbols). This allows to quantify the energy W_{visc} lost in viscoelastic dissipation (blue line).

In the case where no other energy losses than elastic waves radiation or viscoelastic dissipation occur, we predicted that the ratios $W_{el}/\Delta E_c$ and $W_{visc}/\Delta E_c$ should increase and tend towards 100% when the mass m increases and decreases, respectively [equations (38) and (39)]. Here, elastic waves radiation and viscoelastic dissipation follow the same dependence on the mass than that predicted but represent respectively from 0.03% to 5% and from 2% to 40 % of the lost energy ΔE_c only (Figure 14). For impacts on rough substates as the two blocks investigated here, but also on the field, it is therefore important to take into account the energy W_{other} lost in other processes. In our experiments, this energy seems to be an increasing percentage of the lost energy ΔE_c, from 50% to more than 99%, as the bead mass m increases (Figure 14).

4.4.3. Evaluation of the Energy Budget for Natural Rockfalls

The energy budget of impacts on rough blocks in our laboratory experiments can be used to extrapolate that of natural rockfalls. On the field, the impactors masses varies from a few grams to a few tons and drop heights varies from a few centimeters to several tens of meters. Owing to strong energy dissipation in such complex media, only impacts of

large masses can be detected by seismic methods. Viscoelastic dissipation should therefore be negligible in most situations encountered on the field. For example, we can estimate the energy lost in viscoelastic dissipation for a granite gravel of $m = 100$ g impacting the ground with impact speed $V_z = 10\ \mathrm{m\ s^{-1}}$ using equation (35) with the coefficient $D = 80$ ns of glass, which has similar properties than granite, and a typical Young's modulus $E_p = 10$ MPa for the ground [*Geotechdata.info*, 2013]. It results that the viscoelastic energy W_{visc} represents only 0.04% of the impact energy E_c, which is negligible. Moreover, it should be even smaller for larger masses m. The energy W_{plast} dissipated in plastic deformation of the ground or of the impactor is expected to be much more significant on the field than in our laboratory experiments and even more so when the mass m increases because large stresses are applied on damaged materials with a low yield stress. For such impacts with a rough contact, the energy W_{plast}, in addition to other energy lost in rotation and translational modes of the impactor, should then represent almost all of the lost energy ΔE_c (see Appendix C). Consequently, the ratio of the radiated elastic energy over the lost energy $W_{el}/\Delta E_c$ may not exceed a few percents. For example, for impacts of beads on the rough concrete block, for which plastic deformation is significant, the ratio $W_{el}/\Delta E_c$ seems to saturate to $2\% \pm 1\%$ for $m \simeq 1$ g and then decreases (Figure 14a).

5. Discussion

5.1. Discrepancy from Hertz's Model

The characteristic frequencies of the signal generated by an impact do not significantly deviate from *Hertz* [1882]'s prediction when the impact is inelastic (Figure 9). On the contrary, in some experiments, the measured radiated elastic energy W_{el} diverges from that (noted W_{el}^{th}) given by the scaling laws in Table 1 (Figures 7 and 8). As a consequence,

the masses m and speeds V_z retrieved from the measured signal in our experiments using the elastic model deviate from their real values (Figure 10). Let us discuss here the observed discrepancy.

5.1.1. Small Bead Diameters

On smooth thin plates, for small bead diameters, viscoelastic dissipation is the major energy loss process (Figure 12). For a steel bead of diameter 1 mm impacting the glass plate, using equation (19) with $D = 35$ ns (see Table 5), the coefficient C_{plate} is found to be equal to 1.15 instead of 1.21 for an elastic impact (see Figure 2a). Thus, the viscoelastic impact theory predicts that the radiated elastic energy W_{el}^{th} should be only of 5% smaller than for an elastic impact, which is negligible compared with the observed difference of 73% (Figure 7g).

The major source of discrepancy is probably due to the fact that our sensors are band limited up to 50 kHz. Indeed, for the 1-mm bead, 50% of the radiated energy is in theory higher than 50 kHz (see Appendix B). The remaining 23% may be lost in adhesion of the bead on the plate during the impact. In addition, some energy may be lost in electrostaticity or capillarity, which are greater for the smallest beads [*Andreotti et al.*, 2013]. The discrepancy is totally explained by the limited bandwidth of the accelerometers for a steel bead of diameter $d = 2$ mm on the glass plate: about 30% of the energy is over 50 kHz and the measured energy W_{el} is 35% smaller than W_{el}^{th} (Figure 7g). Similarly, on concrete, for a steel bead of diameter $d = 2$ mm, the theory predicts that only 17% of the radiated elastic energy is below 50 kHz. As a consequence, the measured energy W_{el} represents only 17% of the theoretical energy W_{el}^{th} (Figure 8c). For greater bead diameters, both measured and theoretical energies are contained below 50 kHz and the agreement

753 with elastic theory is better (Figures 7 and 8). In contrast, on marble the radiated elastic
754 energy is closer to the theory for the smallest beads (Figures 13d to 13f). For small bead
755 diameters, less wave reflections occur within the block and the measured energy may
756 therefore be overestimated because the diffuse field is not completely set [*Farin et al.*,
757 2015].

758 This emphasize the importance for future applications to use seismic sensors sensitive
759 in the widest frequency range as possible. In cases where we can not measure the highest
760 frequencies of the seismic vibration generated by an impact, note that it is possible to
761 retrieve the momentum mV_z of the impactor from the low frequency content of measured
762 amplitude spectrum (see Appendix D).

763 **5.1.2. Large Bead Diameters**

764 On smooth thin plates, the divergence of the measured radiated elastic energy W_{el} from
765 the theoretical one W_{el}^{th} for large bead diameters is partly compensated when we take into
766 account the decrease of the coefficient C_{plate} when the parameter λ_Z increases (Figures
767 2a and 11). However, in some experiments, W_{el} is still smaller than the theory when the
768 bead diameter d is larger than the plate thickness h (Figures 11c, 11d and 11f). This
769 difference may be due to plastic deformation which is more likely to occur for the largest
770 beads investigated.

771 **5.1.3. Impacts with a Rough Contact**

772 Two complementary effects can explain the discrepancy of the measured radiated elastic
773 energy with theory for impacts of spherical beads on the two rough blocks and for impacts
774 of gravels (Figures 7d, 7h and 8).

First, plastic deformation is a likely cause for measuring a smaller radiated elastic energy than in theory on the blocks. If $P_Y/P_0 = 0.6$ in the elasto-plastic model, the radiated elastic energy predicted in Table 1 is two times smaller than for an elastic impact because the coefficient $C_{block} \approx 0.01$ instead of 0.02 (Figure 2b). This factor of 2 corresponds to that observed between the measured energy W_{el} and the theoretical one W_{el}^{th} for impacts of glass and steel beads on the concrete block (Figures 8a and 8c). Measuring the discrepancy of the radiated elastic energy from elastic theory could then be a mean to estimate the dynamic yield strength P_Y of a material. For example, for a steel bead of diameter $d = 5$ mm dropped from height $H = 10$ cm on concrete, the maximum stress is $P_0 \approx 300$ MPa and, if $P_Y/P_0 = 0.6$, the dynamic yield strength would be $P_Y \approx 180$ MPa, which is greater than the typical values of P_Y for concrete [20-40 MPa, *The Engineering Toolbox*, 2014] but of the same order of magnitude.

An additional process can accommodate the discrepancy. If a spherical bead impacts a rough surface or as a gravel impacts a flat surface, the equivalent radius of contact may be smaller than the radius of the impactor (Figure 15). Table 1 shows that the radiated elastic energy W_{el} increases with the impactor radius R as R^5 on plates and as R^3 on blocks. Then, if the radius of contact R is only 1.15 smaller on plates, the theoretical radiated elastic energy W_{el} is two times smaller, and this explain the discrepancy observed for gravels on the plates (Figures 7d and 7h). On blocks, if the effective radius of contact R is 2.1 times smaller, the radiated elastic energy W_{el} is 10 times smaller, that could explain the small energy values measured on the marble block (Figures 8e to 8h). The radius of contact R should be even smaller when gravels impacts the rough blocks and the radiated elastic energy W_{el} is then smaller (Figures 8d and 8h). By comparison, the characteristic

798 frequencies f_{mean} and Δf are inversely proportional to the radius R (because $T_c \propto R$)
799 and are therefore less affected by a change in this radius than the radiated elastic energy
800 W_{el}. This is visible on Figure 9 because the frequencies of the signal emitted by gravels
801 are close to that of spherical beads.

802 As the effective radius of contact decreases for a given mass m, the stresses are con-
803 centrated on a smaller area during the impact and plastic deformation is more likely to
804 occur (see Appendix C). Interestingly, even though the energy lost in plastic deformation
805 is very important for impacts of gravels and on the rough blocks, the measured radiated
806 elastic energy W_{el} and frequencies f_{mean} and Δf still follow well the scaling laws in mass
807 m and impact speed V_z predicted using Hertz's model of impact of a sphere on a plane
808 (Figures 7, 8 and 9). Therefore, we expect that Hertz's model should be still valid at
809 first order on the field and, consequently, that the radiated elastic energy W_{el} should be
810 proportional to $mV_z^{13/5}$ and that the characteristic frequencies f_{mean} and Δf should be
811 proportional to $1/T_c \propto m^{-1/3}V_z^{1/5}$. The problem is however to determine the coefficients
812 of proportionality in these relations because they depend on the rheological parameters
813 of the impactor and the ground (Table 1), on the fact that is impact is elastic or inelastic
814 (Figures 2 and 3) and on the roughness of contact, which are each extremely difficult to
815 estimate practically. A solution may be to calibrate the coefficients of proportionality of
816 these relations on a given site by dropping some boulders of known mass m and estimat-
817 ing their impact speed V_z. Once calibrated, these laws can be inverted as in section 2.2.3
818 and used to retrieve the masses m and impact speeds V_z of other rockfalls on the same
819 site from the generated seismic signals. The advantage of this method is that it is not
820 necessary to know the elastic parameters of the ground. Even so, energy attenuation as a

function of frequency during wave propagation within the substrate need to be evaluated in order to correct the measured signals.

5.2. Errors on the Estimation of the Masses and Impact Speeds

Here we comment the errors on our estimation of the impactors masses from measured seismic signals in Figure 10. These errors are greater than that of *Buttle et al.* [1991] who managed to size sub-millimetric particles in a stream with a standard deviation less than 10%. However, their estimations were based on the impact force and duration on the direct compressive wave, measured at the opposite of the impact on the target block. Practically, this method is difficult to apply on the field because seismic stations are at the surface. Furthermore, the force and duration of the impact are more complicated to estimate from the seismic signal than the radiated elastic energy and the frequencies because it requires a deconvolution process that induce additional errors [e.g., *McLaskey and Glaser*, 2010]. Our method has the advantage to be not intrusive and in principle exportable to field problems.

5.3. Application to Natural Rockfalls

Dewez et al. [2010] conducted field scale drop experiments of individual basalt boulders on a rock slope in Tahiti, French Polynesia. The main objective of this study was to estimate hazards associated with rockfalls in a volcanic context. Boulders trajectory was optically monitored using two cameras with 50 frames per seconds. A photogrammetry technique then allowed the authors to compute the position of each boulder in time with an error smaller than the boulder radius [*Dewez et al.*, 2010]. In parallel, the seismic signal generated by boulders impacts on the ground was recorded with a sampling frequency of

841 100 Hz by a board band seismometer type *STS* located a few tens of meters away. Here
842 we want to observe how the elastic energy radiated by boulder impacts scales with the
843 boulder's mass and speed in this natural context.

844 **5.3.1. Comparison of Field Measurements with Hertz's Prediction**

845 The waves generated by the impacts propagate in a very damaged and complex medium
846 that may involve several layers of different density. In this medium, viscous attenuation
847 of energy can be very strong, especially for high frequencies. For example, waves of
848 frequency 100 Hz only propagate in the first centimeters or meters deep below the surface.
849 Knowing the attenuation as a function of frequency, and assuming some sensitivity /
850 noise level for the sensor, it is possible to correct for this attenuation for all frequencies
851 where the amplitude is above the noise level. The corrected amplitude spectrum should
852 then be equivalent to the emitted spectrum, assuming that all the frequencies have been
853 recorded. The attenuation of energy as a function of frequency can be evaluated, for
854 example, by measuring the signal emitted by a given impact at different distances, as we
855 did in our laboratory experiments [*Farin et al.*, 2015]. Unfortunately, no estimation of
856 the attenuation has been conducted in this field study. We therefore assume a classical
857 attenuation model of energy with distance r and multiply the measured signals by the
858 factor $\exp(\gamma(f)r)$, with $\gamma(f) = \pi f/Qc_R$ [*Aki and Richards*, 1980]. We use the quality
859 factor $Q = 10$, which is of the order of the values obtained by *Ferrazzini and Aki* [1992]
860 in the similar context of Kilauea volcano in Hawaï.

861 We first focus on the seismic signals emitted by the impacts of a boulder of mass $m = 326$
862 kg at $r \simeq 30$ m from the seismometer (Figure 16a). The signals have a short duration
863 ~ 0.8 s and are impulsive, as the ones generated by bead impacts (e.g., Figure 6c). The

impacts excite a frequency range from $\sim$ 10 Hz to 40 Hz (Figure 16b). Most of the recorded seismic spectra lies between 10 Hz and 20 Hz with a peak frequency $f_{peak} \approx 15.5$ Hz, a mean frequency $f_{mean} \approx 18.4$ Hz and a bandwidth $\Delta f \approx 18.3$ Hz (Figures 16b and 16c).

We compare the measured spectrum with a synthetic amplitude spectrum predicted by *Hertz* [1882]'s theory of impact using equation (2). The Green's function used in the computation depends on the excited mode. *Deparis et al.* [2008], *Dammeier et al.* [2011] and *Lévy et al.* [2015] showed that rockfall events generate principally Rayleigh surface waves. Rayleigh waves develop in far field, i.e. for $kr >> 1$, where $k = 2\pi f/c_R$ is the wave number [*Miller and Pursey*, 1954; *Gimbert et al.*, 2014; *Farin et al.*, 2015]. In the Piton de la Fournaise volcano, Reunion Island, where the ground has a similar structure as in Tahiti, the phase speed c_R is 800 m s^{-1} [*Hibert et al.*, 2011]. We use here the same phase speed c_R and estimate that $kr >> 1$ when the frequency f is greater than about 4 Hz. Since the recorded seismic energy is mostly between 10 Hz to 40 Hz, we can therefore reasonably use the far field Green's function of Rayleigh waves of equation (4) convolved with *Hertz* [1882]'s impact force to compute the synthetic spectrum (Figure 16c).

The characteristics of the impactor are $R = 0.35$ m, $m = 326$ kg and $V_z = 11$ m s^{-1}. We assume a typical Young's modulus $E_p = 10$ MPa for a loose soil such that observed on the slope [*Geotechdata.info*, 2013]. *Hertz* [1882]'s elastic theory then predicts that the duration of impact should be $T_c \simeq 0.035$ s [equation (9)]. For Rayleigh surface waves, the mean frequency should therefore be $f_{mean} = 1/T_c \simeq 28$ Hz and the bandwidth $\Delta f = 0.6/T_c \simeq 17$ Hz, which are close to the measured values (Table 2 and Figure 16c).

886 The amplitude of the synthetic spectrum is similar to that of the measured spectrum
887 except around 15 Hz where a peak of energy is observed in the measured spectrum (Figure
888 16c). The peak of energy may be due to a resonance around 15 Hz of the seismometer or
889 of the first sediment layers because it is observed on every measured spectra [*Schmandt*
890 *et al.*, 2013; *Farin*, 2015]. The shape of the measured and synthetic spectrum is very
891 different. This may be due to plastic deformation, which is very important for impacts
892 on loose and fractured soil.

893 **5.3.2. Elastic Energy Radiated by Boulders Impacts**

894 Despite the discrepancy between the theory and the measurement, we observe how the
895 elastic energy W_{el} radiated by the impacts of all boulders depends on the boulder mass
896 m and impact speed V_z. The calculation of W_{el} is based on the integration of the energy
897 flux over a cylinder surrounding the impacts [*Hibert et al.*, 2011; *Farin et al.*, 2015]:

898 $$W_{el} = 4\pi r h \rho c_R \int_0^{+\infty} |\tilde{V}(r,f)|^2 \exp\left(\gamma(f) r\right) \mathrm{d}f, \tag{44}$$

899 where $h = c_R/f$ is the Rayleigh wavelength and $|\tilde{V}(r,f)|^2 = |\tilde{V}_X(r,f)|^2 + |\tilde{V}_Y(r,f)|^2 +$
900 $|\tilde{V}_Z(r,f)|^2$ is the sum of the squared time Fourier transforms of the vibration speeds in
901 the three directions of space $v_X(r,t)$, $v_Y(r,t)$ and $v_Z(r,t)$, respectively. The coefficient
902 $\gamma(f) = \pi f/Qc_R$ is the same than that used to compute the synthetic spectrum in the
903 previous section, with $c_R = 800$ m s^{-1} and $Q = 10$.

904 The nature of the contact between the boulder and the ground during the impact plays
905 a crucial role on the transfer of the seismic energy. Therefore, we separated the "hard"
906 impacts, occurring on outcropping rock, from the "soft" impacts, occurring on loose soil
907 or on grass (Figures 16d to 16g). The measured radiated elastic energy W_{el} seems to be
908 proportional to the mass m as predicted analytically for impacts on thick blocks (Table 1

and Figure 16d). This dependance is clearer for "soft" impacts. However, the measured radiated elastic energy W_{el} does not scale well with the parameter $mV_z^{13/5}$ derived from Hertz's theory (Figure 16e). We adjust the power a of parameter mV_z^a to obtain a better fit with W_{el}. The best fit is observed for power $a \simeq 0.5$, i.e. with a much weaker dependence on the impact speed V_z than in theory, with $W_{el} \propto {V_z}^{0.5}$ rather than $W_{el} \propto {V_z}^{13/5}$ (Figure 16f). The scaling law in $V_z^{0.5}$ may be biased because boulders systematically impacted loose soil when they reached high speeds V_z while they often impacted outcropping rocks for lower speeds V_z. The energy transfer is lower for "loose" impacts than for "hard" impacts and this may then leads to the observed weaker dependence in V_z (Figure 16g). As a matter of fact, the mean ratio of the radiated elastic energy W_{el} over the kinetic energy ΔE_c lost during the impacts is one order of magnitude higher for "hard" impacts than for "soft" impacts (Figure 16g). Interestingly, the ratio $W_{el}/\Delta E_c$ is between 10^{-4} and 10^{-1}, which is in agreement with the values observed by *Hibert et al.* [2011].

No clear dependence on m and V_z was observed for the characteristic frequencies of the signal f_{mean} and Δf. These frequencies are between 10 Hz and 30 Hz, regardless of the contact quality i.e., of the fact that the impact is "hard" or "soft" [see Figure 92 in Chapter 4 of *Farin*, 2015].

An explanation for the discrepancy between observed and theoretical elastic energy W_{el} and for the fact that we did not observe any trend for the frequencies may be that we can not record frequencies higher than 50 Hz because the sampling frequency is 100 Hz. Impacts of boulders are expected to generate waves of higher frequencies. For example, *Helmstetter and Garambois* [2010] dropped a boulder of similar dimensions on the Séchilienne rockslide site in the French Alps. Seismic signals generated by the impacts

were sampled at 250 Hz by several seismic stations located a few tens of meters away. In the spectrogram of these signals, energy is visible up to 100 Hz. As we previously observed in laboratory experiments, when we do not measure the highest frequencies of the generated signal, the discrepancy between the theory and the measurement increases (e.g. for small masses m in Figures 8a to 8c). An other possibility is that the factor $\exp(\gamma(f)r)$, with $\gamma(f) = \pi f/Qc_R$, may be too simple to describe the wave propagation is such a damaged medium. Indeed, multiple modes with different dispersion relations can be excited in different frequencies range in such layered media. However, the data are not sufficient to determine how wave disperse and attenuate within the ground on this specific site.

Owing to the large scattering of the seismic data, it is difficult to neither validate nor invalidate the applicability on the field of the analytical scaling laws developed in this paper. However, this study highlights several challenges that need to be addressed in order to be able to retrieve the impacts parameters in future seismic studies of boulder impacts. If the radiated elastic energy or the characteristics frequencies of the emitted signals are underestimated, this will lead to either overestimate or underestimate the masses and impact speed, as evidenced in our laboratory experiments (Figure 10). Therefore, one should measure as much as possible the entire energy spectrum emitted by the impacts and, to do so, use a high sampling frequency, ideally greater than $3/T_c$ (see section 2.2.2). Moreover, because energy at high frequencies attenuate very rapidly in fractured media, one should record the signal a close as possible from the impacts. Finally, one should have a good knowledge of the elastic properties of the impactor and the ground in the vicinity of the impact, as well as within the ground i.e., its how it disperses and attenuates the

frequencies. This could be achieved using several seismic stations recording at different distances from the source.

6. Conclusions

We developed analytical scaling laws relating the characteristics of the acoustic signal generated by an impact on a thin plate and on a thick block (radiated elastic energy, frequencies) to the parameters of the impact: the impactor mass m and speed before impact V_z and the elastic parameters. These laws were validated with laboratory experiments of impacts of spherical beads of different materials and gravels on thin plates with a smooth surface, which is an ideal case, and on rough thick blocks, which are closer to the case of the field. Viscoelastic and elasto-plastic dissipation occurred in the range of masses and impact speeds investigated. In these experiments, the radiated elastic energy is estimated from vibration measurements, independently of the other processes of energy dissipation. A number of conclusions can be drawn from our results:

1. The impactor mass m and speed V_z can be estimated from two independent parameters measurable on the field of the seismic signal: the radiated elastic energy and a characteristic frequency, using equations (27) to (30). The estimations of m and V_z are close to the real values within a factor of 2 and 3, respectively, even when the impactor has a complex shape. If the radiated elastic energy is underestimated (respectively, overestimated) by a factor of 10, the mass m and the impact speed V_z are underestimated (respectively, overestimated) by a factor of 1.5 and 2, respectively. We noted that the radiated elastic energy is smaller when the surface roughness increases because the radius of contact is smaller. However, the signal characteristics measured during impacts of

rough impactors on rough surfaces follows well the scaling laws established for impacts of spherical beads on a plane surface.

2. We also established a quantitative energy budget of the impacts on the plates and blocks investigated and we estimated what should be this budget for naturals rockfalls:

(i) On the smooth plates, elastic waves and viscoelastic dissipation are the main processes of energy losses. Viscoelastic dissipation is major for impactors of diameter less than 10% of the plate thickness while elastic waves radiation represents only from 0.1% to 0.3% of the impact energy. When the bead diameter increases, the energy lost in viscoelastic dissipation decreases while the energy radiated in elastic waves increases. For beads of diameter larger than the plate thickness, almost all of the energy is radiated in elastic waves.

(ii) On the rough blocks, elastic dissipation represents only between 0.03% and 5% of the lost energy. In contrast, energy lost in other processes such as plastic deformation increases with the bead mass from 50% to more than 99% of the lost energy because of surface roughness. The energy dissipated in viscoelasticity decreases from 50% to 2% of the lost energy as the bead mass increases.

(iii) Most of the energy lost during a natural rockfall should be dissipated in plastic deformation or in translational or rotational modes of the impactors. Plastic or in general irreversible dissipation reduces the energy radiated in elastic waves and is difficult to quantify. That said, regardless of the impactor mass and speed, the energy radiated in elastic waves may not be more than a few percent of the impact energy. Energy lost in viscoelastic dissipation should be negligible in the range of masses detected by seismic stations on the field.

The impacts experiments with rough impactors on rough substrates demonstrated that Hertz's model can be used to describe at first order the dynamics of an impact when the contact surface is not plane. Thus, we expect that the simple analytical relations derived in this paper between the characteristics of the impact and that of the emitted signal can allow us to better understand the process of elastic waves generation by impacts on the field. The major limitation for estimating the impact properties from the signal on the field would certainly be the fact that a great part of the radiated energy is lost in high frequencies during wave propagation in highly fractured media. Therefore, we encourage future seismic studies of rockfalls to record signals as close as possible to the impacts and to use a high frequency sampling. In addition, it is important to correct measured seismic signals from wave dispersion and attenuation within the substrate. If these conditions are fulfilled, the scaling laws derived in this study should provide estimates of the order of magnitude of the masses and speeds of the impactors. Finally, in addition to direct field applications, the scaling laws developed for plates can be also useful in the industry as a non-intrusive technique to estimate the size and speed of particles in a granular transport and in shielding problems.

Appendix A: Demonstration of the Analytical Scaling Laws for the Radiated Elastic Energy

The objective of this Appendix is to demonstrate the analytical scaling laws showed in Table 1 for the radiated elastic energy W_{el} as a function of the impactor's mass m and speed V_z for thin plates and thick blocks.

The radiated elastic energy is defined by:

$$W_{el} = \int_{-\infty}^{+\infty} |F_z(t)|^2 Y_{el}(t) \mathrm{d}t = 2 \int_0^{+\infty} |\tilde{F}_z(f)|^2 \tilde{Y}_{el}(f) \mathrm{d}f, \tag{A1}$$

with $\tilde{Y}_{el}(f)$ the radiation admittance, that has a different expression on thin plates and on thick blocks.

A1. Thin Plates

On thin plates, $\tilde{Y}_{el}(f)$ is independent of frequency f and is given by:

$$Y_{el} = \frac{1}{8\sqrt{B\rho_p h}}. \tag{A2}$$

where B is the bending stiffness and ρ_p and h are the plate density and thickness, respectively.

Therefore,

$$W_{el} = \frac{1}{8\sqrt{B\rho_p h}} \frac{F_0^2 \delta_{z0}}{V_z} \int_{-\infty}^{+\infty} |g(t^*)|^2 \mathrm{d}t^*, \tag{A3}$$

with $t^* = \delta_{z0} t / V_z$ and where $g(t^*)$ is the shape function represented on Figures 1b and 1c. The integral in this equation is noted C_{plate} and depends on the inelastic parameters α and P_Y/P_0 i.e., of the fact that the impact is elastic, viscoelastic or elasto-plastic (Figures 2a and 2b). For an elastic impact, $C_{plate} = 1.21$.

Developing F_0 and δ_{z0} as functions of the impact parameters using their expressions in equations (5) and (8), respectively, we get:

$$\frac{F_0^2 \delta_{z0}}{V_z} = \left(\frac{4}{3}\right)^{1/3} \left(\frac{5}{4}\right)^{8/5} \pi^{-1/15} \rho_s^{-1/15} E^{*2/5} m^{5/3} V_z^{11/5}. \quad \text{(A4)}$$

Finally, equations (A3) and (A4) give the scaling law relating the radiated elastic energy W_{el} to the impact parameters on thin plates:

$$W_{el} = a_1 C_{plate} m^{5/3} V_z^{11/5}, \quad \text{(A5)}$$

with $a_1 \approx 0.18 E^{*2/5}/(\rho_s^{1/15}\sqrt{B\rho_p h})$.

A2. Thick Blocks

On thick blocks, the radiation admittance $\tilde{Y}_{el}(f)$ was computed in time Fourier domain by *Miller and Pursey* [1955]:

$$\tilde{Y}_{el}(f) = \frac{2\pi\xi^4 \beta f^2}{\rho_p c_P^3}, \quad \text{(A6)}$$

where $\xi = \sqrt{2(1-\nu_p)/(1-2\nu_p)}$, c_P is the compressive wave speed and β is the imaginary part of

$$\int_0^X \frac{x\sqrt{x^2-1}}{f_0(x)} \mathrm{d}x, \quad \text{(A7)}$$

with $f_0(x) = (2x^2-\xi^2)^2 - 4x^2\sqrt{(x^2-1)(x^2-\xi^2)}$ and X, a real number greater than the positive real root of f_0. The coefficient β depends only on the Poisson's ratio ν_p (Figure 17, see the Appendix of *Farin et al.* [2015] for details on the computation of β).

Therefore,

$$W_{el} = \frac{4\pi\xi^4\beta}{\rho_p c_P^3} \frac{F_0^2 V_z}{\delta_{z0}} \int_0^{+\infty} f^{*2} |\tilde{g}(f^*)|^2 \mathrm{d}f^*, \quad \text{(A8)}$$

with $f^* = V_z f/\delta_{z0}$ and $\tilde{g}(f^*)$ is the time Fourier transform of the function $g(t^*)$ represented on Figures 1b and 1c. We note C_{block} the integral in this equation. C_{block} depends on the

inelastic parameters α and P_Y/P_0 (Figures 2a and 2b). With an impact force $F_z(t)$ given by *Hertz* [1882]'s elastic theory i.e., for $\alpha = 0$ and $P_Y/P_0 = 1$, we have $C_{block} = 0.02$.

If we develop F_0 and δ_{z0} as functions of the impact parameters, we get:

$$\frac{F_0^2 V_z}{\delta_{z0}} = \frac{4}{3}\left(\frac{5}{4}\right)^{4/5} \pi^{-1/5} \rho_s^{-1/5} E^{*6/5} m V_z^{13/5}. \tag{A9}$$

Finally, inserting equation (A9) into equation (A8) we obtain the analytical expression of the radiated elastic energy W_{el} on thick blocks:

$$W_{el} = a_2 C_{block} m V_z^{13/5}, \tag{A10}$$

with the coefficient $a_2 \approx 15.93 \xi^4 \beta E^{*6/5} / (\rho_p \rho_s^{1/5} c_P^3)$.

Appendix B: Cumulative Distribution of Energy

In this Appendix, we show how the radiated elastic energy radiated by impacts is distributed over the frequencies.

The cumulative distribution of the radiated elastic energy shows that impacts generate signals with higher frequencies as the bead diameter d decreases, regardless of the structure (Figure 18). It is clear that the sensors used in our experiments do not measure energy for frequencies higher than 50 kHz. This is not a problem for impacts on the PMMA plate and for beads of diameter d larger than 5 mm because all of the radiated elastic energy is in theory below 50 kHz (Figure 18a). However, for impacts of beads of 1 mm in diameter on glass, concrete and marble, more than 50% of the energy is for frequencies higher than 50 kHz (Figures 18b to 18d). Some of the radiated energy may not be measured for the smallest beads investigated. Note that for experiments on the glass plate and on the concrete and marble blocks, the profile of the cumulative energy is steep and saturates

to a given frequency $f \approx 38$ kHz, $f \approx 30$ kHz and $f \approx 40$ kHz, respectively, as the bead diameter d decreases (Figures 18b to 18d).

Appendix C: Influence of the Impactor Shape on the Energy Budget

In this Appendix, we investigate the energy budget of impacts of gravels on the glass plate.

When a spherical bead is dropped without initially speed and rotation on a smooth surface it rebounds almost vertically and without spin. In contrast, a rough gravel rebounds to a much smaller height and can reach a large horizontal distance x with a high rotation speed ω_r up to about 400 rad s^{-1}, depending on the face it lands on (Figure 19a). For these complex impactors, the kinetic energy converted in translational and rotational modes is therefore not negligible. The translational kinetic energy of rebound is $E_c' = \frac{1}{2}mV'^2$ where $V' = V_x'\mathbf{u}_x + V_z'\mathbf{u}_z$ is the rebound speed in the cartesian frame $(0, \mathbf{u}_x, \mathbf{u}_z)$. $V_x' \approx 0$ cm s^{-1} for spherical beads but varies from 5 cm s^{-1} to 40 cm s^{-1} for gravels. The rotation energy is $E_\omega = \frac{1}{2}I\omega_r^2$, where I is the moment of inertia of the gravel, given by $I = \frac{2}{5}mR^2$ if we assume that the gravel is spherical with an equivalent radius R. From camera recordings, we estimate that $32\% \pm 17\%$ of the impact energy E_c is converted into translational energy of rebound E_c' and that $13\% \pm 11\%$ is converted into rotational energy E_ω. Regardless of the shape and mass m of the gravel, less energy is converted into translational energy E_c' as its rotates faster after the impact (Figure 19b). The percentage of energy radiated in elastic waves W_{el}/E_c is $3.3\% \pm 1.8\%$ and seems independent of the energy converted in translation energy E_c'/E_c or in rotational modes E_ω/E_c (Figures 19c and 19d).

In section 4.4.1, we adjusted the inelastic parameter D on the variation of the coefficient of restitution e to estimate the energy lost in viscoelastic dissipation (Figure 12). This

1094 is not possible for gravels because of the large dispersion in the results. As granite has
1095 similar elastic properties than glass, we assume that D is the same than for glass beads
1096 impacts on the glass plate i.e., $D = 80$ ns (see Table 5). Therefore, the viscoelastic
1097 dissipation W_{visc} for impacts of gravels on the glass plate may represent $3.7\% \pm 1\%$ of E_c.
1098 The rest of the energy ($48\% \pm 14\%$) is lost to deform plastically the gravel and or the
1099 glass plate. This is therefore the main process of energy dissipation for gravels impacts.

1100 The proportion of energy radiated in elastic waves W_{el}/E_c seems to decrease when
1101 more energy is lost in plastic deformation (Figure 19e), which is in agreement with the
1102 elasto-plastic model (Figure 2a).

Appendix D: Determining Impactor Momentum from Low Frequencies

1103 In some experiments on Figure 10, the estimations of m and V_z are affected because
1104 the highest frequencies of the generated vibration are not measured by the sensors or
1105 because of a resonance. The purpose of this Appendix is to show that we can use the low
1106 frequencies content of the signal to estimate the momentum mV_z of the impactor.

1107 For frequencies $f \sim 0$ Hz, we assume as *Tsai at al.* [2012] that the impact duration T_c
1108 is instantaneous relative to the frequencies of interest. The time Fourier transform $\tilde{F}(f)$
1109 of the *Hertz* [1882] force $F(t)$ then becomes constant in frequency:

1110 $$\tilde{F}(f) = \int_{-\infty}^{+\infty} F(t) \exp(-ift) \mathrm{d}t \sim \int_{-\infty}^{+\infty} F(t) \mathrm{d}t. \tag{D1}$$

1111 where, if we normalize the force $F(t)$ by its maximum value F_0 and time t by the impact
1112 duration T_c and develop their respective expressions [equations (9) and (10)],

1113 $$\int_{-\infty}^{+\infty} F(t) \mathrm{d}t \approx 2mV_z. \tag{D2}$$

The amplitude spectrum of the vibration acceleration can then be approximated by [*Aki and Richards*, 1980]:

$$|\tilde{A}_z(r, f \to 0)| \sim 2mV_z(2\pi f)^2|\tilde{G}_{zz}(r, f)|. \quad \text{(D3)}$$

Using the expression of the Green's function $|\tilde{G}_{zz}(r, f)|$ given by equations (3) and (4) on plates and blocks, respectively, we show that:

$$|\tilde{A}_z(r, f \to 0)| \sim af^b, \quad \text{(D4)}$$

with $a \approx 0.73mV_z\frac{1}{B\sqrt{r}}(\frac{B}{\rho_p h})^{5/8}$ and $b = 3/4$ on plates and $a \approx 100mV_z\frac{\xi^2}{\mu c_P}\frac{\sqrt{x_0(x_0^2-1)}}{f_0'(x_0)}\sqrt{\frac{2c_P}{\pi r}}$ and $b = 5/2$ on blocks.

In order to determine the momentum mV_z of a steel bead of diameter 5 mm dropped from height 10 cm on the glass plate and on the concrete block, we adjust the power law (D4) with the measured spectra $|\tilde{A}_z(r, f)|$ for frequencies $f < 10$ kHz (Figure 20). The obtained momentum is $mV_z \approx 6.9.10^{-4}$ kg m s^{-1} on glass plate and $mV_z \approx 6.33.10^{-4}$ kg m s^{-1} on the concrete block, which is in good agreement with the real momentum $mV_z \approx 6.85.10^{-4}$ kg m s^{-1}. Finally, if either m or V_z is known, this method can be used to estimate the other parameter.

Notation

c_P, c_R	Compressional and Rayleigh waves speed (m s^{-1})
D	Viscoelastic coefficient (s)
d, R	Bead diameter and radius (m)

E_c Initial kinetic energy (J)

E_s, E_p, ν_s, ν_p Young's modulii (Pa) and Poisson's coefficients of the sphere and the plane

E^* Equivalent Young's modulus (Pa)

e Coefficient of restitution (-)

$\mathbf{F}$, F_z Force and normal force (N)

F_0, P_0 Maximum force and stress of elastic impact (N; Pa)

F_{max}, δ_{max} Maximum force and penetration depth of inelastic impact (N)

f, ω Frequency and angular frequency (s^{-1})

f_{peak}, f_{mean}, Δf Peak, mean frequencies and bandwidth (Hz)

g Acceleration of gravitation (m s^{-2})

H Height of fall (m)

h Plate thickness (m)

K Parameter in *Hertz* [1882]'s theory

k Wave number (m^{-1})

V Volume (m^3)

m Mass (kg)

r Distance from the impact (m)

T_c Impact duration (s)

t Time (s)

$\mathbf{u}_i$ Normalized vector of the direction i

v_i, a_i Vibration speed and acceleration in the direction $\mathbf{u}_i$ (m s^{-1}; m s^{-2})

$\tilde{V}_i$, $\tilde{A}_i$ Time Fourier transform of v_i and a_i, respectively (m; m s^{-1})

V_z, V' Impact speed and speed after rebound (m s^{-1})

v_g, v_ϕ Group and phase velocities (m s^{-1})

W_{el}, ΔE_c	Radiated elastic energy and total energy lost (J)
W_{el}^{th}, $W_{el}^{th'}$	Theoretical radiated elastic energy predicted by *Hertz* [1882]'s and *Zener* [1941]'s models (J)
W_{visc}, W_{other}, E'_c, E_ω	Energy lost in viscoelastic dissipation, in other processes, kinetic energy of rebound and rotation (J)
x, y, z	Coordinates in the cylindric reference frame of the block (m)
Y_d, P_d	Dynamic yield stress and dynamic yield strength (Pa)
α	Viscoelastic parameter (-)

β, ξ, C_{plate}, C_{block}, C_{visc}	Coefficients involved in energy calculation (-)
γ	Attenuation coefficient of energy with distance (m^{-1})
δ_z, δ_{z0}	Penetration depth and maximum of this depth during the impact (m)
λ_Z	*Zener* [1941]'s parameter (-)
ρ_s, ρ_p	Densities of the sphere and the plane (kg m^3)
τ	Characteristic time of energy attenuation within the structure (s)
χ, η	Bulk and shear viscosities (Pa s)
ω_r	Rotation speed (rad s^{-1})

Acknowledgments. We thank E. Falcon, A. Valance, Y. Forterre, D. Royer, A. Schubnel, T. Reuschlé and L. Jouniaux for helpful discussions. We are indebted to A. Steyer for technical help. We thank Aude Nachbaur, Hiromi Kobayashi, Christophe Rivière, Em-

manuel Des Garets and Emilie Nowak for assistance in rockfall experiments in Tahiti. We are grateful to Florent Gimbert and an anonymous reviewer for their interesting comments to our initial manuscript. This work was supported by the european project ERC SLIDEQUAKES and the Agence Nationale de la Recherche ANR LANDQUAKES, REALISE and ITN FLOWTRANS.

References

Aki, K., and P. Richards (1980), *Quantitative Seismology : Theory and Methods*, vol. 1, W.H. Freeman.

Allstadt, K. (2013), Extracting source characteristics and dynamics of the August 2010 Mount Meager landslide from broadband seismograms, *J. Geophys. Res.*, *118*(3), doi: 10.1002/jgrf.20110.

Andreotti, B., Y. Forterre, and O. Pouliquen (2013), *Granular Media: Between Fluid and Solid, vol. 1*, Cambridge Univ. Press.

Brilliantov, N. V., F. Spahn, J.-M. Hertzsch, and T. Pöschel (1996), Model for collisions in granular gases, *Phys. Rev. E*, *53*, 5382–5392, doi:10.1103/PhysRevE.53.5382.

Burtin, A., L. Bollinger, J. Vergne, R. Cattin, and J. L. Nábělek (2008), Spectral analysis of seismic noise induced by rivers: A new tool to monitor spatiotemporal changes in stream hydrodynamics, *J. Geophys. Res.*, *113*(B5), B05,301, doi: 10.1029/2007JB005034.

Buttle, D. J., and C. B. Scruby (1990), Characterization of particle impact by quantitative acoustic emission, *Wear*, *137*(1), 63–90, doi:10.1016/0043-1648(90)90018-6.

1152 Buttle, D. J., S. R. Martin, and C. B. Scruby (1991), Particle sizing by quantitative
1153 acoustic emission, *Res. Nondestruct. Eval.*, *3*(1), 1–26, doi:10.1007/BF01606508.
1154 Crook, A. W. (1952), A study of some impacts between metal bodies by a piezo–lectric
1155 method, *Philos. T. Roy. Soc. A*, *212*(1110), 377–390, doi:10.1098/rspa.1952.0088.
1156 Dammeier, F., J. R. Moore, F. Haslinger, and S. Loew (2011), Characterization of alpine
1157 rockslides using statistical analysis of seismic signals, *J. Geophys. Res.*, *116*(F4), doi:
1158 10.1029/2011JF002037.
1159 Davies, R. M. (1949), The determination of static and dynamic yield stresses using a steel
1160 ball, *P. Roy. Soc. Lond. A Mat.*, *197*(1050), 416–432, doi:10.1098/rspa.1949.0073.
1161 Deparis, J., D. Jongmans, F. Cotton, L. Baillet, F. Thouvenot, and D. Hantz (2008),
1162 Analysis of rock-fall and rock-fall avalanche seismograms in the French Alps, *Bull.*
1163 *Seism. Soc. Am.*, *98*(4), 1781–1796, doi:10.1785/0120070082.
1164 Dewez, T. J. B., A. Nachbaur, C. Mathon, O. Sedan, H. Kobayashi, C. Rivire, F. Berger,
1165 E. Des Garets, and E. Nowak (2010), OFAI: 3D block tracking in a real-size rock-
1166 fall experiment on a weathered volcanic rocks slope of Tahiti, French Polynesia, *Conf.*
1167 *Proceedings, Rock Slope Stability 2010, 24–25 nov. 2010, Paris, France*, pp. 1–13.
1168 Duran, J. (2010), *Sands, powders and grains: an introduction to the physics of granular*
1169 *materials*, Boston Academic Press.
1170 Falcon, E., C. Laroche, S. Fauve, and C. Coste (1998), Behavior of one inelastic ball bounc-
1171 ing repeatedly off the ground, *Eur. Phys. J. B*, *3*(1), 45–57, doi:10.1007/s100510050283.
1172 Farin, M. (2015), Études expérimentales de la dynamique et de l'émission sismique des
1173 instabilités gravitaires, Ph.D. thesis, IPGP, Paris.

1174 Farin, M., A. Mangeney, J. de Rosny, R. Toussaint, J. Sainte-Marie, and N. Shapiro
1175 (2015), Experimental validation of theoretical methods to estimate the energy radiated
1176 by elastic waves during an impact, *(submitted)*.

1177 Favreau, P., A. Mangeney, A. Lucas, G. Crosta, and F. Bouchut (2010), Numerical mod-
1178 eling of landquakes, *Geophys. Res. Let.*, *37*, doi:10.1029/2010GL043512.

1179 Ferrazzini, V., and K. Aki (1992), *Volcanic Seismology: Preliminary Results from a Field*
1180 *Experiment on Volcanic Events at Kilauea Using an Array of Digital Seismographs*,
1181 168–189 pp., Springer-Verlag Berlin.

1182 Geotechdata.info (2013), Soil young's modulus, *http://www.geotechdata.info/parameter/soil-*
1183 *young%27s-modulus.html*, accessed: 2015-20-04.

1184 Gimbert, F., V. C. Tsai, and M. P. Lamb (2014), A physical model for seismic noise
1185 generation by turbulent flow in rivers, *J. Geophys. Res. Earth Surf.*, *119*, 2209–2238,
1186 doi:10.1002/2014JF003201.

1187 Goyder, H., and R. G. White (1980), Vibrational power flow from machines into built-
1188 up structures, part I: introduction and approximate analyses of beam and plate-like
1189 foundations, *J. Sound Vib.*, *68*(1), 59–75, doi:10.1016/0022-460X(80)90452-6.

1190 Helmstetter, A., and S. Garambois (2010), Seismic monitoring of Séchilienne rockslide
1191 (French Alps): Analysis of seismic signals and their correlation with rainfalls, *J. Geo-*
1192 *phys. Res.*, *115*(F3), F03,016, doi:10.1029/2009JF001532.

1193 Hertz, H. (1882), Über die Berührung fester elastischer Körper (On the vibration of solid
1194 elastic bodies), *J. Reine Angew. Math.*, *92*, 156–171, doi:10.1515/crll.1882.92.156.

1195 Hertzsch, J., F. Spahn, and N. V. Brilliantov (1995), On low-velocity collisions of vis-
1196 coelastic particles, *J. Phys. II France*, *5*(11), 1725–1738, doi:10.1051/jp2:1995210.

1197 Hibert, C., A. Mangeney, G. Grandjean, and N. M. Shapiro (2011), Slope instabilities
1198 in Dolomieu crater, Réunion Island: From seismic signals to rockfall characteristics, *J.*
1199 *Geophys. Res.*, *116*(F4), F04,032, doi:10.1029/2011JF002038.
1200 Hibert, C., A. Mangeney, G. Grandjean, C. Baillard, D. Rivet, N. M. Shapiro, C. Satriano,
1201 A. Maggi, P. Boissier, V. Ferrazzini, and W. Crawford (2014a), Automated identifica-
1202 tion, location, and volume estimation of rockfalls at piton de la fournaise volcano, *J.*
1203 *Geophys. Res.*, *119*(5), 1082–1105, doi:10.1002/2013JF002970.
1204 Hibert, C., G. Ekström, and C. Stark (2014b), Dynamics of the Bingham
1205 Canyon Mine landslides from seismic signal analysis, *Geophys. Res. Let.*, *41*, doi:
1206 10.1002/2014GL060592.
1207 Hunter, S. C. (1957), Energy absorbed by elastic waves during impact, *J. Mech. Phys.*
1208 *Solids*, *5*(3), 162–171, doi:10.1016/0022-5096(57)90002-9.
1209 Israelachvili, J. (2002), *Intermolecular and surface forces: third edition*, Springer Verlag,
1210 New York.
1211 Johnson, K. (1985), *Contact Mechanics*, Cambridge University Press.
1212 Kanamori, H., and J. W. Given (1982), Analysis of long-period seismic waves excited by
1213 the May 18, 1980, eruption of Mount St. Helens – A terrestrial monopole, *J. Geophys.*
1214 *Res.*, *87*, 5422–5432, doi:10.1029/JB087iB07p05422.
1215 Kuwabara, G., and K. Kono (1987), Restitution coefficient in a collision between two
1216 spheres, *Jpn. J. Appl. Phys.*, *26*(8R), 1230.
1217 Lévy, C., A. Mangeney, F. Bonilla, C. Hibert, E. Calder, P. Smith, and P. Cole (2015),
1218 Friction weakening in granular flows deduced from seismic records at the Souffrière Hills
1219 Volcano, Montserrat, *(submitted)*.

1220 Mayeda, K., and L. Malagnini (2010), Source radiation invariant property of local and
1221 near-regional shear-wave coda: Application to source scaling for the Mw 5.9 Wells,
1222 Nevada sequence, *Geophys. Res. Lett.*, *37*(7), doi:10.1029/2009GL042148.

1223 McLaskey, G. C., and S. D. Glaser (2010), Hertzian impact: Experimental study of
1224 the force pulse and resulting stress waves, *J. Acoust. Soc. Am.*, *128*(3), 1087, doi:
1225 10.1121/1.3466847.

1226 Miller, G. F., and H. Pursey (1954), The field and radiation impedance of mechanical
1227 radiators on the free surface of a semi-infinite isotropic solid, *Proc. R. Soc. Lond. A.*
1228 *Mat.*, *223*(1155), 521–541, doi:10.1098/rspa.1954.0134.

1229 Miller, G. F., and H. Pursey (1955), On the partition of energy between elastic
1230 waves in a semi-infinite solid, *Proc. R. Soc. Lond. A. Mat.*, *233*(1192), 55–69, doi:
1231 10.1098/rspa.1955.0245.

1232 Moretti, L., A. Mangeney, Y. Capdeville, E. Stutzmann, C. Huggel, D. Schneider, and
1233 F. Bouchut (2012), Numerical modeling of the Mount Steller landslide flow history
1234 and of the generated long period seismic waves, *Geophys. Res. Lett.*, *39*(16), doi:
1235 10.1029/2012GL052511.

1236 Moretti, L., K. Allstadt, A. Mangeney, Y. Capdeville, E. Stutzmann, and F. Bouchut
1237 (2015), Numerical modeling of the Mount Meager landslide constrained by its force
1238 history derived from seismic data, *J. Geophys. Res.: Solid Earth*, *120*(4).

1239 Norris, R. D. (1994), Seismicity of rockfalls and avalanches at three cascade range vol-
1240 canoes: Implications for seismic detection of hazardous mass movements, *Bull. Seism.*
1241 *Soc. Am.*, *84*(6), 1925–1939.

Ramírez, R., T. Pöschel, N. V. Brilliantov, and T. Schwager (1999), Coefficient of restitution of colliding viscoelastic spheres, *Phys. Rev. E*, *60*(4), 4465–4472, doi: 10.1103/PhysRevE.60.4465.

Reed, J. (1985), Energy losses due to elastic wave propagation during an elastic impact, *J. Phys. D Appl. Phys.*, *18*(12), 2329, doi:10.1088/0022-3727/18/12/004.

Royer, D., and E. Dieulesaint (2000), *Elastic Waves in Solids I: Free and Guided Propagation*, Springer.

Sánchez-Sesma, F. J., R. L. Weaver, H. Kawase, S. Matsushima, F. Luzon, and M. Campillo (2011), Energy Partitions among Elastic Waves for Dynamic Surface Loads in a Semi-Infinite Solid, *Bull. Seism. Soc. Am.*, *101*(4), 1704–1709, doi: 10.1785/0120100196.

Schmandt, B., R. C. Aster, D. Scherler, V. C. Tsai, and K. Karlstrom (2013), Multiple fluvial processes detected by riverside seismic and infrasound monitoring of a controlled flood in the Grand Canyon, *Geophys. Res. Lett.*, *40*, 4858–4863, doi:10.1002/grl.50953.

Suriñach, E., I. Vilajosana, G. Khazaradze, B. Biescas, G. Furdada, and J. M. Vilaplana (2005), Seismic detection and characterization of landslides and other mass movements, *Nat. Hazards Earth Syst. Sci.*, *5*(6), 791–798, doi:10.5194/nhess-5-791-2005.

The Engineering Toolbox (2014), Concrete properties, < *http* : *//www.engineeringtoolbox.com/concrete − properties − d*_1223.*html* >, accessed: 11-20-14.

Tillett, J. (1954), A study of the impact of spheres on plates, *Proc. Phys. Soc. B*, *67*(9), 677, doi:10.1088/0370-1301/67/9/304.

Troccaz, P., R. Woodcock, and F. Laville (2000), Acoustic radiation due to the inelastic impact of a sphere on a rectangular plate, *J. Acoust. Soc. Am.*, *108*, 2197, doi: 10.1121/1.1312358.

Tsai, V. C., B. Minchew, M. P. Lamb, and J.-P. Ampuero (2012), A physical model for seismic noise generation from sediment transport in rivers, *Geophys. Res. Lett.*, *39*(2), doi:10.1029/2011GL050255.

Vilajosana, I., E. Suriñach, A. Abellan, G. Khazaradze, D. Garcia, and J. Llosa (2008), Rockfall induced seismic signals: case study in Montserrat, Catalonia, *Nat. Hazards Earth Syst. Sci.*, *8*(4), 805–812, doi:10.5194/nhess-8-805-2008.

Vinningland, J. L., O. Johnsen, E. G. Flekkøy, R. Toussaint, and K. J. Måløy (2007a), Experiments and simulations of a gravitational granular flow instability, *Phys. Rev. E*, *76*, 051,306, doi:10.1103/PhysRevE.76.051306.

Vinningland, J. L., O. Johnsen, E. G. Flekkøy, R. Toussaint, and K. J. Måløy (2007b), Granular rayleigh-taylor instability: Experiments and simulations, *Phys. Rev. Lett.*, *99*, 048,001, doi:10.1103/PhysRevLett.99.048001.

Weaver, R. L. (1985), Diffuse elastic waves at a free surface, *J. Acoust. Soc. Am.*, *78*, doi:10.1121/1.392576.

Yamada, M., Y. Matsushi, M. Chigira, and J. Mori (2012), Seismic recordings of landslides caused by Typhoon Talas (2011), Japan, *Geophys. Res. Lett.*, *39*(13), doi: 10.1029/2012GL052174.

Zener, C. (1941), The intrinsic inelasticity of large plates, *Phys. Rev.*, *59*, 669–673, doi: 10.1103/PhysRev.59.669.

Table 1. Scaling laws for the radiated elastic energy and the energy dissipated in viscoelasticity[a].

	Plates	Blocks
W_{el}	$a_1 C_{plate} m^{5/3} V_z^{11/5}$ $a_3 C_{plate} R^5 H^{11/10}$	$a_2 C_{block} m V_z^{13/5}$ $a_4 C_{block} R^3 H^{13/10}$
W_{visc}	$C_{visc} m V_z^2$ $a_5 C_{visc} R^3 H$	
	$a_1 \approx 0.18 \frac{E^{*2/5}}{\rho_s^{1/15}\sqrt{B\rho_p h}}$	$a_2 \approx 15.93 \frac{\xi^4 \beta E^{*6/5}}{\rho_p \rho_s^{1/5} c_P^3}$
	$a_3 = (2g)^{11/10}(\frac{4}{3}\pi\rho_s)^{5/3} a_1$	$a_4 = (2g)^{13/10}\frac{4}{3}\pi\rho_s a_2$
	$a_5 = 2g\frac{4}{3}\pi\rho_s$	

[a] Radiated elastic energy W_{el} and energy W_{visc} dissipated in viscoelasticity for plates of thickness h and blocks as a function of the impact parameters. The coefficients a_i depend only on the elastic parameters of the impactor and of the structure. The parameter β is a function of the Poisson's ratio ν_p only (see Figure 17 of Appendix A). The coefficients C_{plate} and C_{block} are represented on Figure 2.

Table 2. Characteristics frequencies[a].

	f_{mean}	Δf
plates	$0.75/T_c$	$0.72/T_c$
blocks	$1/T_c$	$0.6/T_c$

[a] Theoretical mean frequency f_{mean} and bandwidth Δf, as respectively defined by equations (25) and (26), of the acoustic signal generated by an elastic impact on a thin plate and on a thick block.

Table 3. Characteristics of the impactors used in experiments: density ρ_s, Young's modulus E_s, Poisson's ratio ν_s, diameter d and mass m.

	material	ρ_s (kg m^{-3})	E_s (GPa)	ν_s -	d (mm)	m (g)
spherical beads	glass	2500	74	0.2	$1-20$	$1.3.10^{-3}-10$
	polyamide	1140	4	0.4	$2-20$	$6.10^{-4}-4.8$
	steel	7800	203	0.3	$1-20$	$4.1.10^{-3}-33$
gravels	granite	3600	60	0.27	$\approx 4-28$	$0.08-18$

Table 4. Characteristics of the materials used in experiments[a]

material		ρ_p (kg m^{-3})	E_p (GPa)	ν_p -	γ (1/m)	τ (s)	v_g (m s^{-1})	v_ϕ (m s^{-1})
glass	$kh < 1$	2500	74	0.2	$0.014 f^{1/6}$	$3.8 f^{-2/3}$	$18.6 f^{1/2}$	$9.3 f^{1/2}$
	$kh > 1$				$8.5 \times 10^{-5} f^{2/3}$		3100	3100
PMMA	$kh < 1$	1180	2.4	0.37	1	$0.09 f^{-1/2}$	$11.7 f^{1/2}$	$5.8 f^{1/2}$
	$kh > 1$				$4.8 \times 10^{-3} f^{2/3}$	$0.15 f^{-2/3}$	1400	1400
concrete	-	2300	16.3	0.4	$2.3.10^{-5} f$	$28 f^{-1}$	1530	1530
marble	-	2800	26	0.3	$2.5.10^{-5} f$	$23.1 f^{-1}$	1750	1750

[a] Density ρ_p, Young's modulus E_p, Poisson's ratio ν_p, characteristic distance $1/\gamma$ and time τ of energy attenuation, group velocity v_g and phase velocity v_ϕ (that depend on the frequency f (in Hz)) [see the supplementary materials of *Farin et al.*, 2015, for details on the measurement of γ and τ].

Table 5. Viscoelastic constant D (in ns)[a]

substrate		PMMA	glass	concrete	marble
bead	glass	230	80	100	180
	polyamide	580	550	300	300
	steel	190	35	200	200

[a] Value of the viscoelastic constant D appearing in equation (19) and adjusted on experimental data for impacts of spherical beads of different material (rows) on the different substrates (columns).

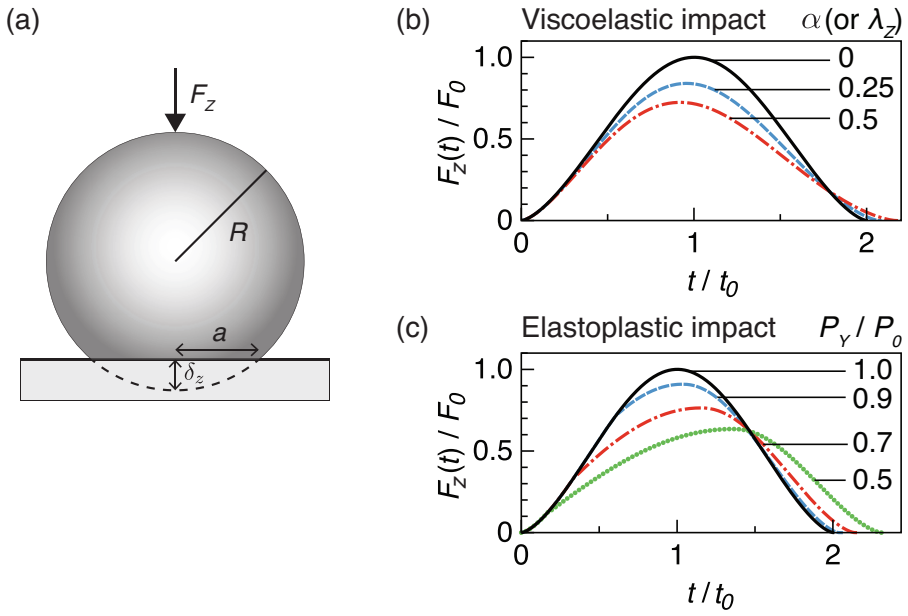

Figure 1. (a) Schematic showing the penetration depth δ_z of a sphere of radius R on a plane surface during an impact. Geometrically, the surface of contact is a circle of radius a. (b) and (c) Normalized force of impact $F_z(t/t_0)/F_0$ for (b) different values of the viscoelastic parameter α (or λ_Z for *Zener* [1941]'s theory; see section 2.1.1.2) and for (c) different values of the stresses ratio P_Y/P_0. F_0 and $t_0 = T_c/2$ are respectively the force and the time at maximal compression during an elastic impact i.e., for $\alpha = 0$ and $P_Y/P_0 = 1$.

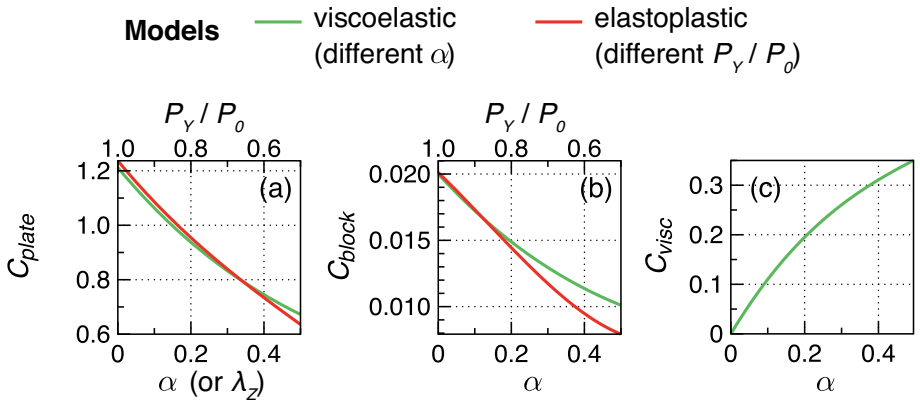

Figure 2. (a), (b) and (c) Values of the constants (a) C_{plate}, (b) C_{block} and (c) C_{visc} as a function of the inelastic parameters α for a viscoelastic impact (or λ_Z for *Zener* [1941]'s theory) (green) and P_Y/P_0 for an elasto-plastic impact (red).

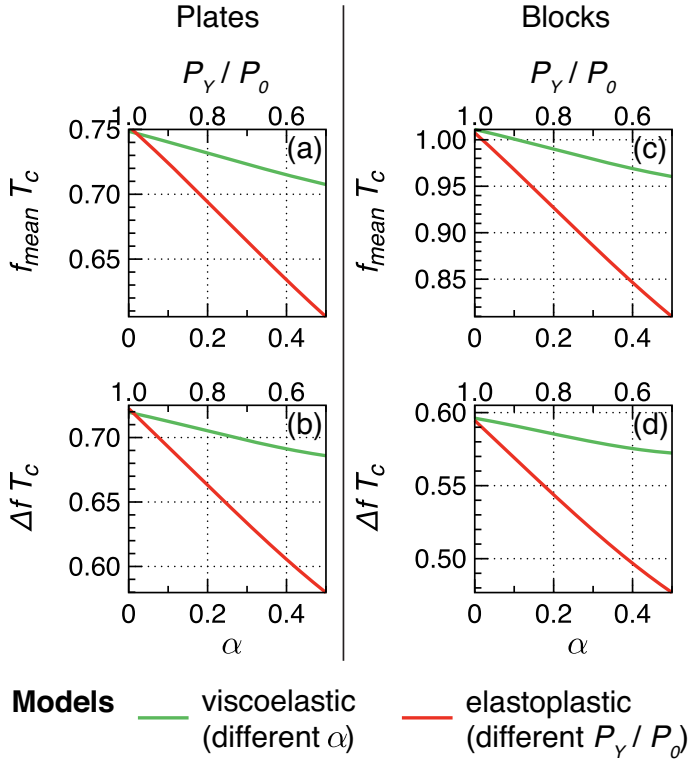

Figure 3. Theoretical values of the (a), (c) mean frequency f_{mean} and (b), (d) bandwidth Δf for (a) and (b) thin plates and (c) and (d) thick blocks, as a function of the inelastic parameters α (green) and P_Y/P_0 (red). All frequencies are multiplied by *Hertz* [1882]'s impact duration T_c to be dimensionless.

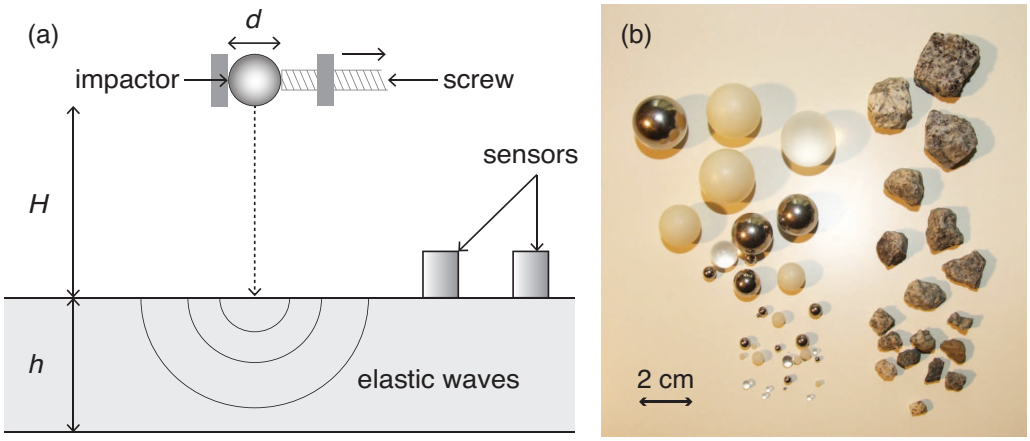

Figure 4. (a) Scheme of the experimental setup. An impactor of diameter d is initially held by a screw and dropped without initial speed or rotation on a hard structure of thickness h. The height of fall H varies from 2 cm to 30 cm. The impact generates elastic waves, recorded by an array of accelerometers. (b) Spherical beads of glass, polyamide and steel and granite gravels used as impactors in the experiments.

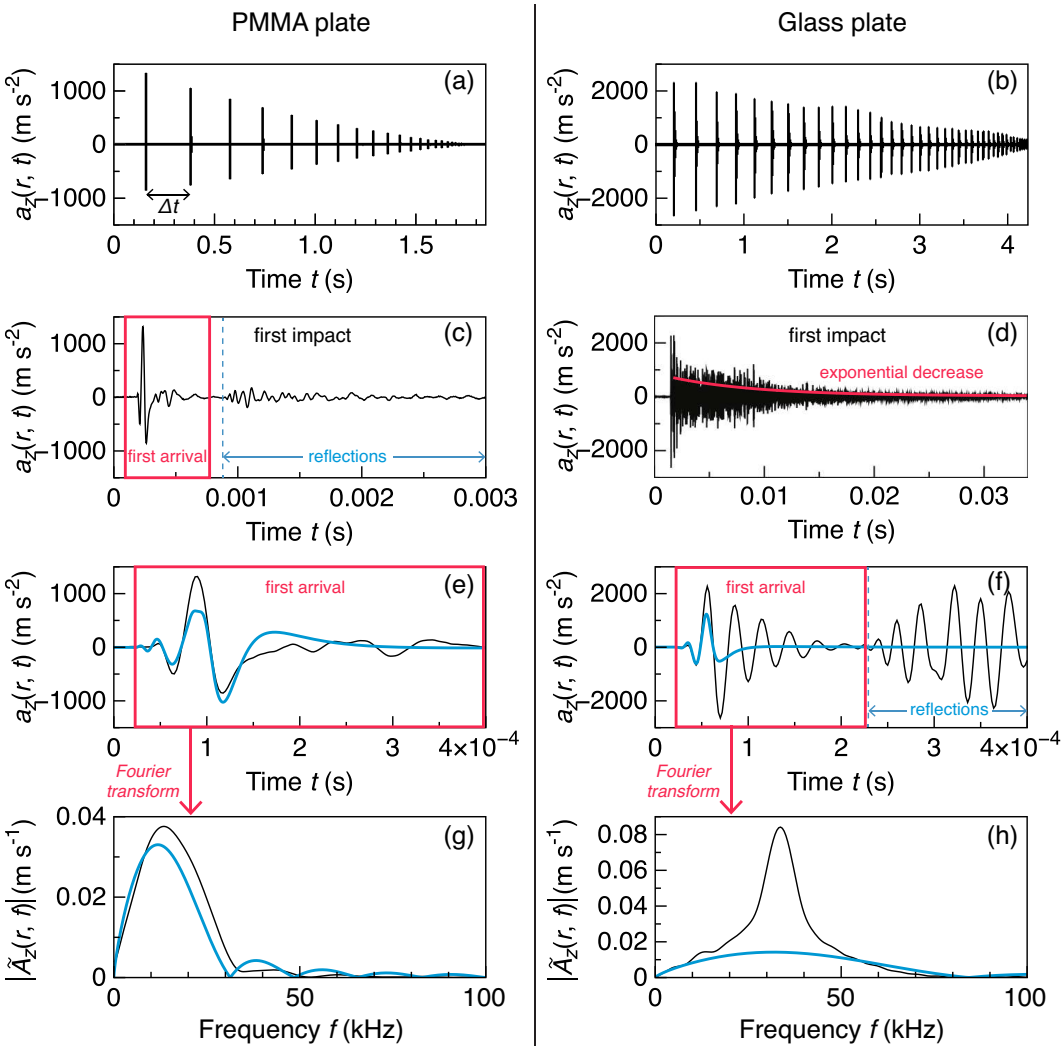

Figure 5. (a) and (b) Acceleration signal $a_z(r,t)$ generated by the successive impacts of a steel bead of diameter $d = 5$ mm, dropped from height $H = 10$ cm on (a) the PMMA plate and (b) the glass plate. The time of flight Δt between two impacts is equal to the duration between two peaks. (c) and (d) Zoom on the signal of the first rebound, filtered below 100 kHz. The coda envelope decreases exponentially with time in the glass plate (red line). (c),(e) and (f) The first arrival is delimited by a red frame and the first reflections off the plate lateral sides arrive at the right of the blue dashed line. The arrival time of the reflections is computed knowing the wave speed and the distance between the sensor and the substrate sides. (g) and (h) The time Fourier transform of the first arrival gives the amplitude spectrum $|\tilde{A}_z(r,f)|$ as a function of the frequency f. The thick blue line in Figures (e) to (h) represents the synthetic signal and amplitude spectrum obtained by convolution of *Hertz*'s [1882] force of impact with the Green's function.

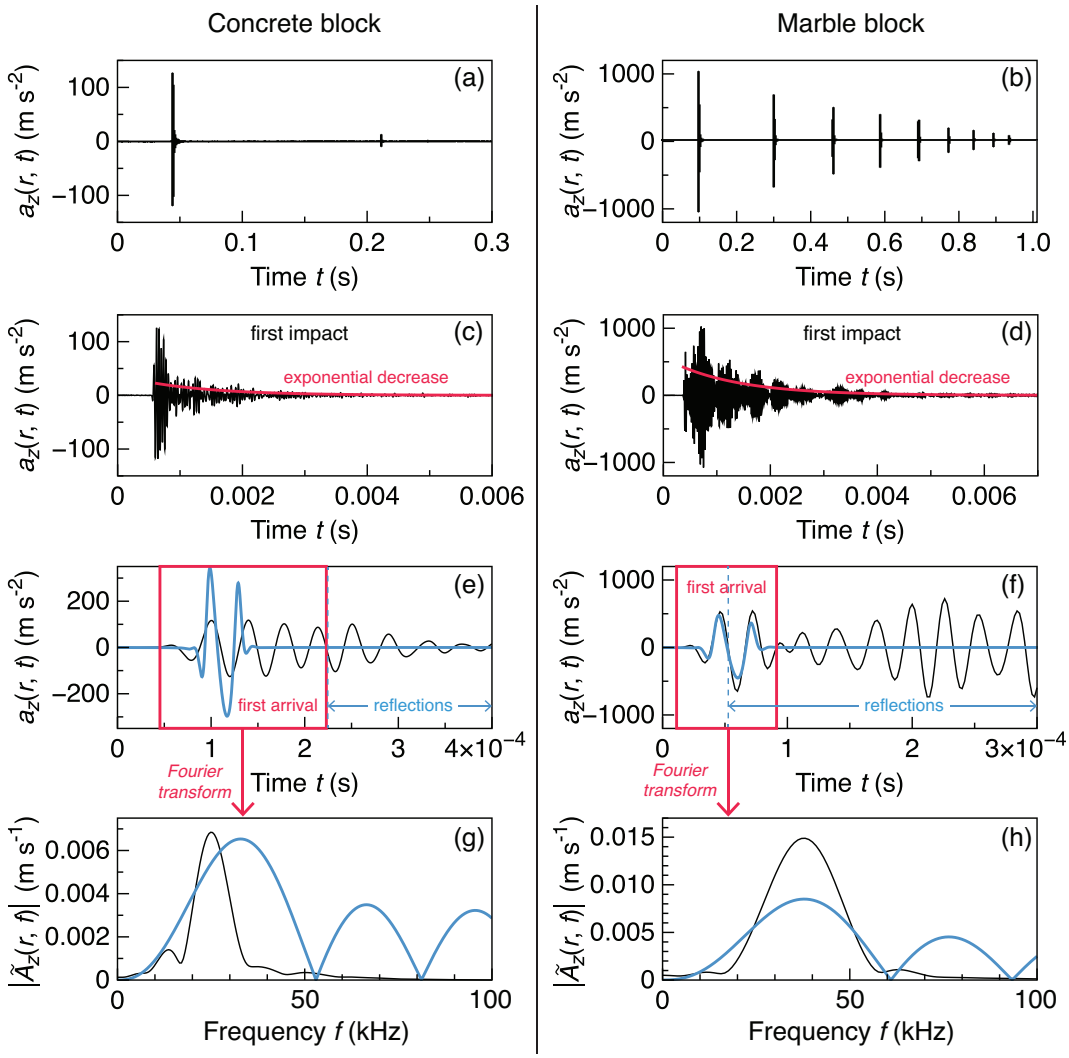

Figure 6. (a) and (b) Acceleration signal $a_z(r,t)$ generated by the successive impacts of a steel bead of diameter $d = 5$ mm, dropped from height $H = 10$ cm on (a) the concrete block and (b) the marble block. (c) and (d) Zoom on the signal of the first rebound, filtered below 100 kHz. The coda envelope decreases exponentially with time (red line). (e) and (f) The first arrival is delimited by a red frame and the first reflections off the plate lateral sides arrive at the right of the blue dashed line. The arrival time of the reflections is computed knowing the wave speed and the distance between the sensor and the substrate sides. (g) and (h) The time Fourier transform of the first arrival gives the amplitude spectrum $|\tilde{A}_z(r,f)|$ as a function of the frequency f. The thick blue line in Figures (e) to (h) represents the synthetic signal and amplitude spectrum obtained by convolution of *Hertz* [1882]'s force of impact with the Green's function.

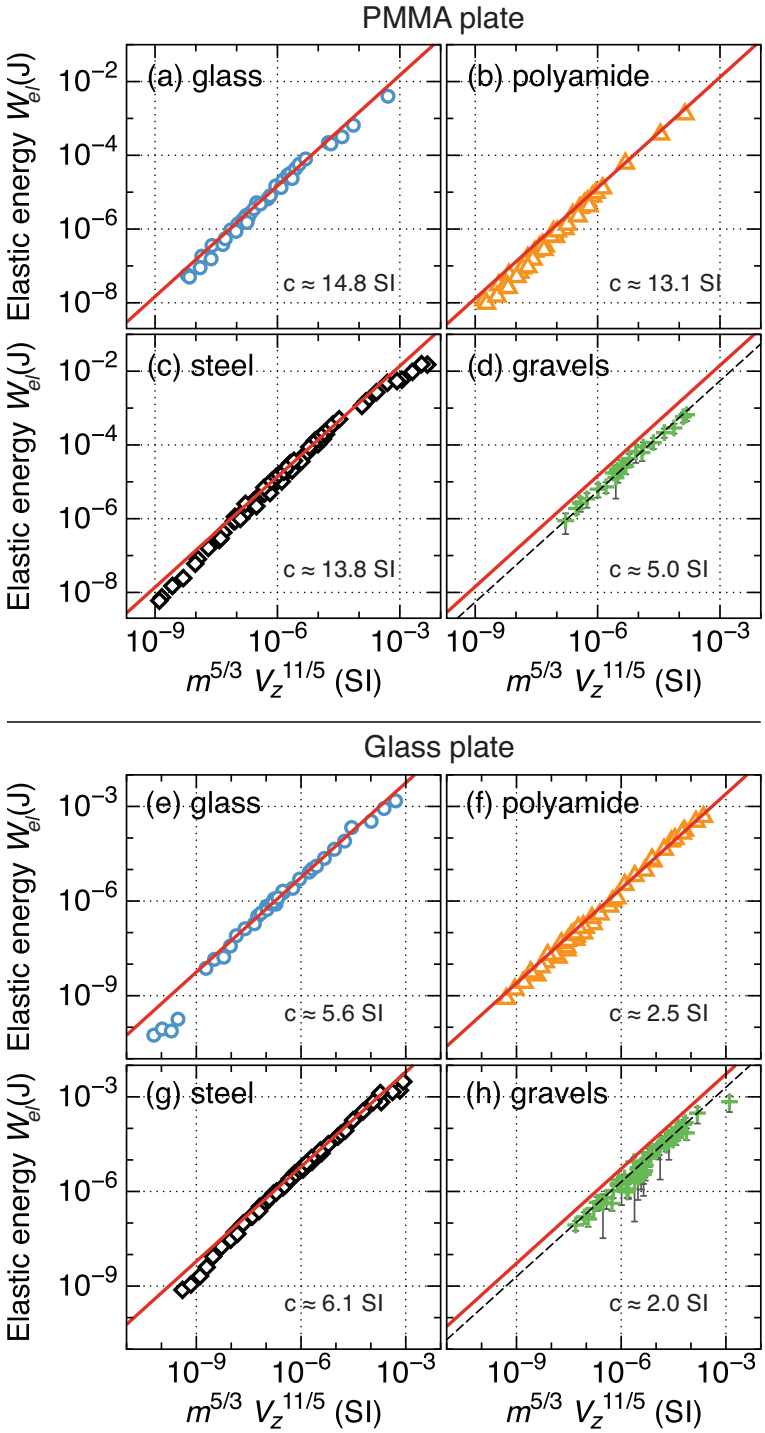

Figure 7. Radiated elastic energy W_{el} as a function of $m^{5/3}V_z^{11/5}$ for impacts of (a)-(e) glass, (b)-(f) polyamide and (c)-(g) steel beads and (d)-(h) gravels on (a) to (d) the PMMA plate and on (e) to (h) the glass plate. The red line corresponds to the theoretical energy W_{el}^{th} given in Table 1 for an elastic impact i.e., with $C_{plate} = 1.21$. The black dashed line is a fit to the data of the law $W_{el} = cm^{5/3}V_z^{11/5}$, with coefficient c indicated in International System Units (SI). In most cases, this line collapses with the theoretical line in red. Error bars on W_{el} ($\pm 35\%$) are computed from ± 1 standard deviation on a series of 20 experiments and are symbols sized.

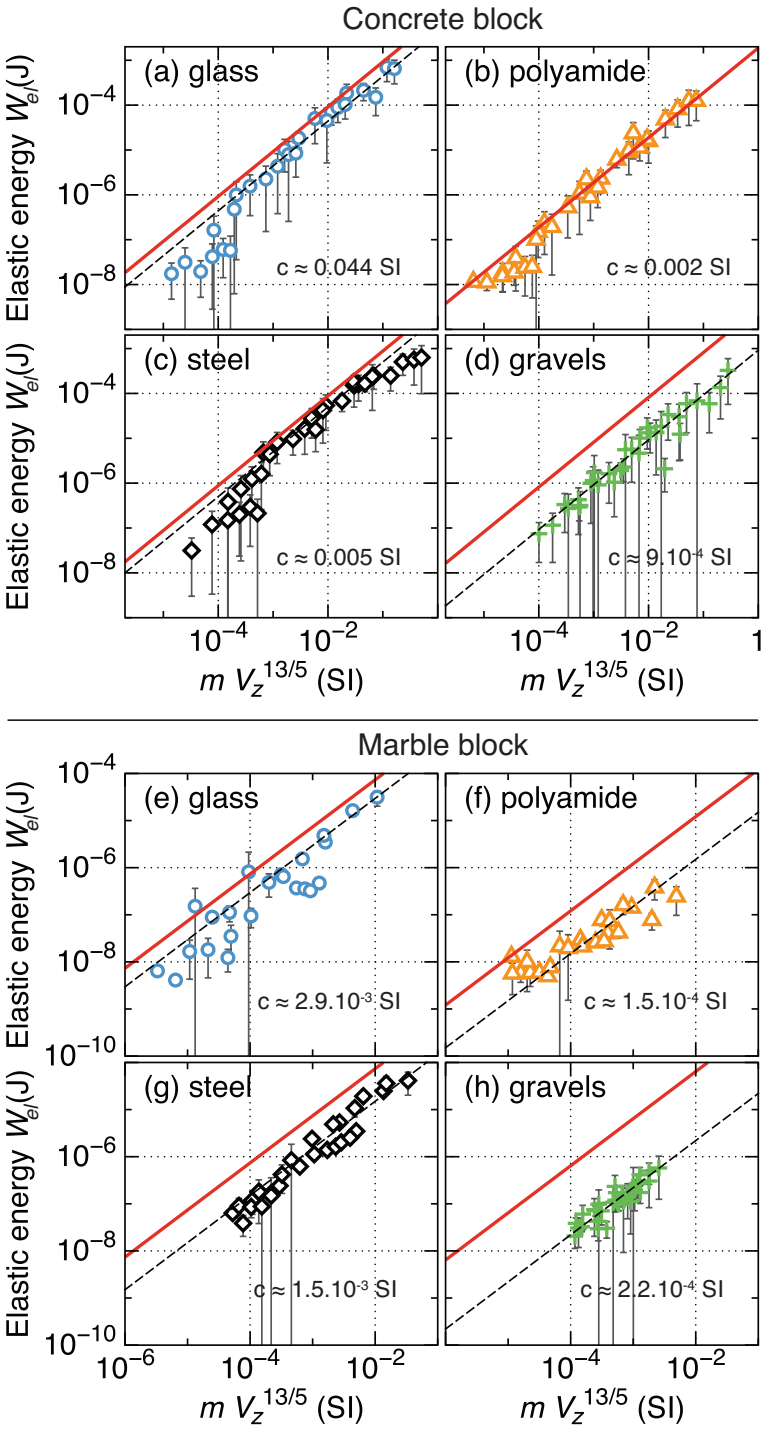

Figure 8. Radiated elastic energy W_{el} as a function of $mV_z^{13/5}$ for impacts of (a)-(e) glass, (b)-(f) polyamide and (c)-(g) steel beads and (d)-(h) gravels on (a) to (d) the concrete block and on (e) to (h) the marble block. The red line corresponds to the theoretical energy W_{el}^{th} given in Table 1 for an elastic impact i.e., with $C_{block} = 0.02$. The black dashed line is a fit to the data of the law $W_{el} = cmV_z^{13/5}$, with coefficient c indicated in International System Units (SI).

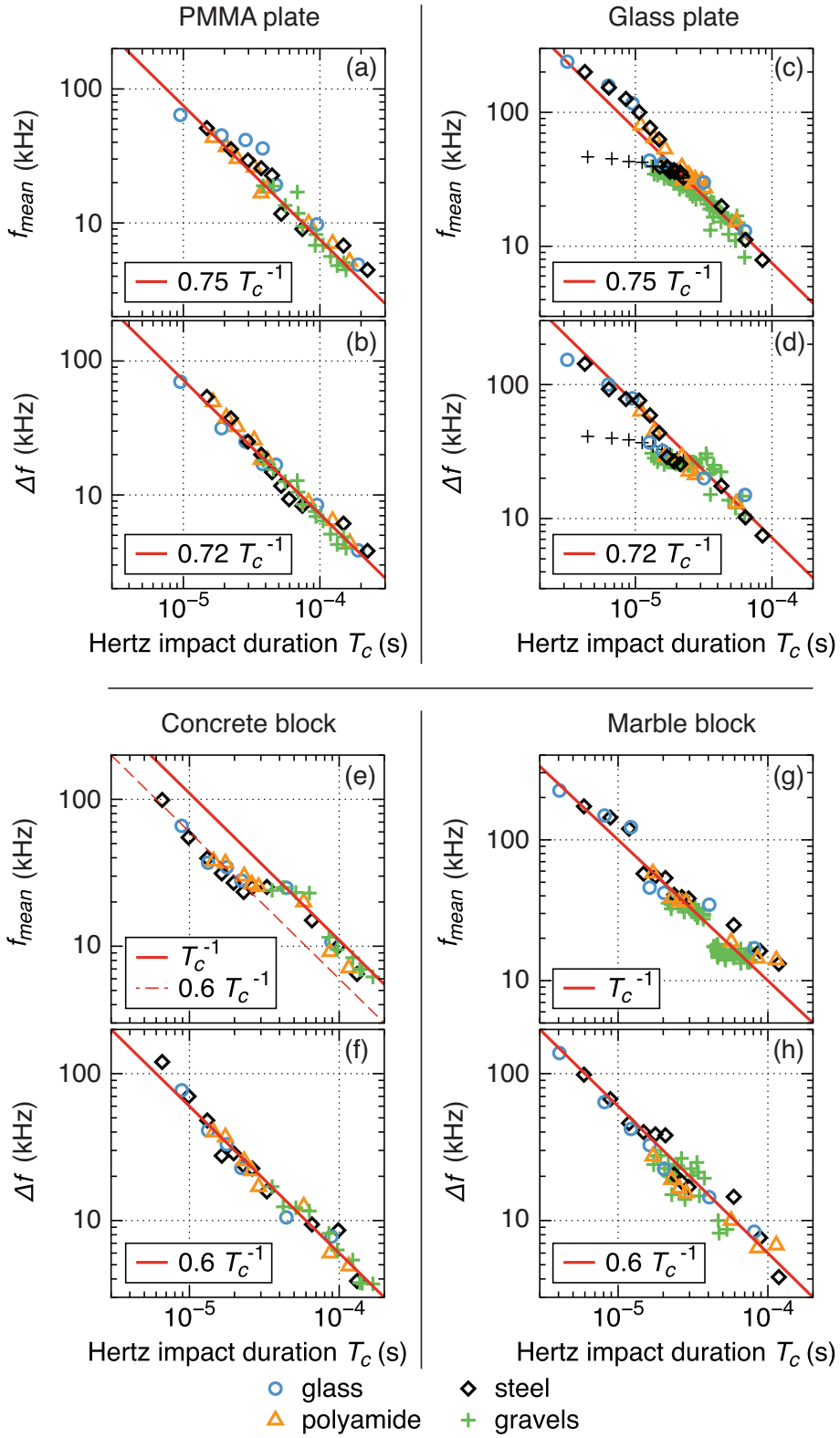

Figure 9. (a), (c), (e) and (g) Mean frequency f_{mean} and (b), (d), (f) and (h) bandwidth Δf as a function of *Hertz* [1882]'s impact duration T_c [equation (9)] for impacts of glass, polyamide and steel beads and granite gravels on (a) and (b) the PMMA plate, (c) and (d) the glass plate, (e) and (f) the concrete block and (g) and (h) the marble block. The red line corresponds to the theoretical prediction (Table 2) and the red dashed line in (e) is a fit to the data. The black crosses on Figures (c) and (d) correspond to the frequencies of the signals generated by steel beads measured with the accelerometers type 8309, that resonate around 38 kHz on the glass

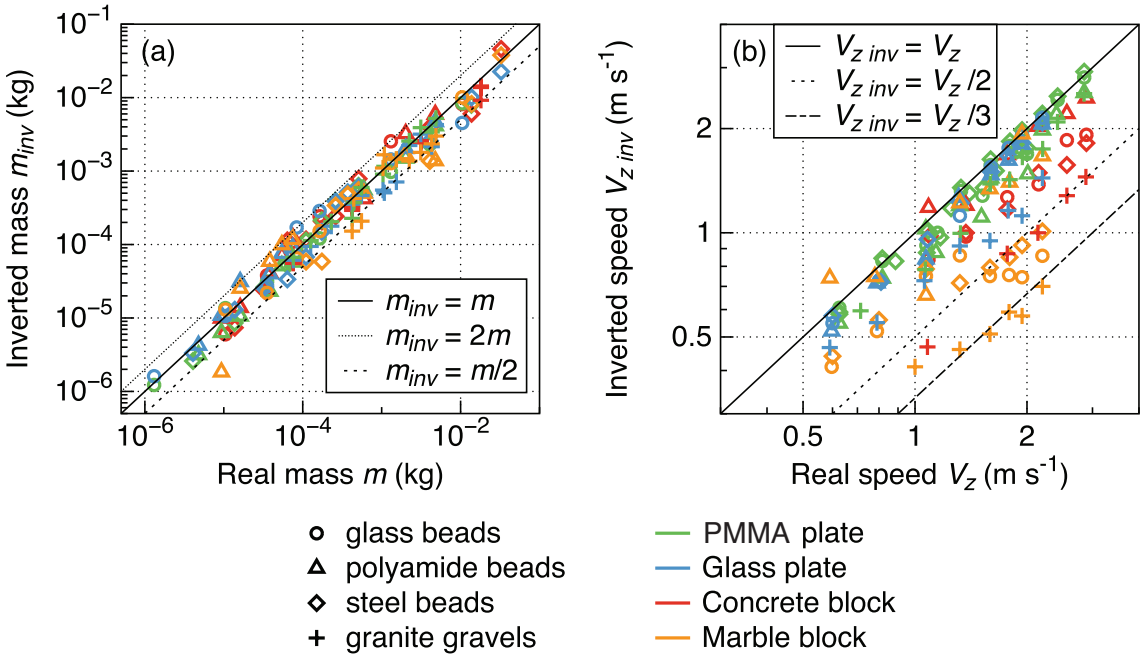

Figure 10. (a) Mass m_{inv} inverted from signal bandwidth Δf and radiated elastic energy W_{el} using equations (27) for plates and (29) for blocks as a function of the real mass m. (b) Impact speed V_{zinv} inverted using equations (28) for plates and (30) for blocks as a function of the real impact speed V_z. The black full line is a perfect fit.

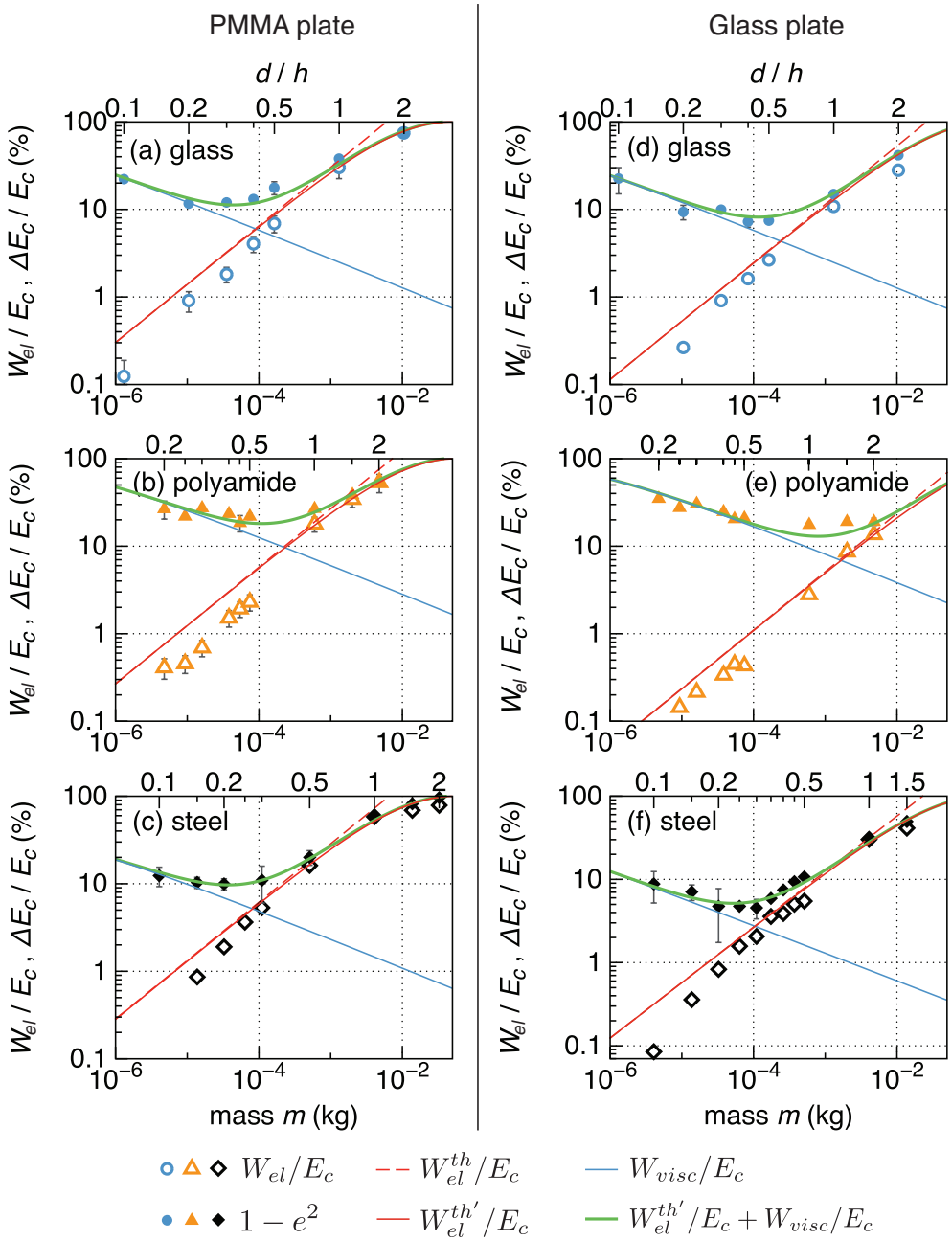

Figure 11. Ratio of the measured radiated elastic energy W_{el} over the impact energy $E_c = \frac{1}{2}mV_z^2$ (empty symbols) and measured lost energy ratio $\Delta E_c/E_c = 1 - e^2$ (full symbols) as a function of bead mass m and of the ratio of the bead diameter d on the plate thickness h for impacts of (a)-(d) glass, (b)-(e) polyamide and (c)-(f) steel beads on (a) to (c) the PMMA plate and on (d) to (f) the glass plate. The red dashed line corresponds to the theoretical ratio W_{el}^{th}/E_c with W_{el}^{th} in equation (23) for an elastic impact i.e., with $C_{plate} = 1.21$. The red full line is the energy ratio $W_{el}^{th'}/E_c$ corrected with C_{plate} dependence on parameter λ_Z, the blue line is the viscoelastic energy ratio W_{visc}/E_c [equation (35)] and the thick green line is the theoretical lost energy ratio, which is the sum of $W_{el}^{th'}/E_c$ and W_{visc}/E_c.

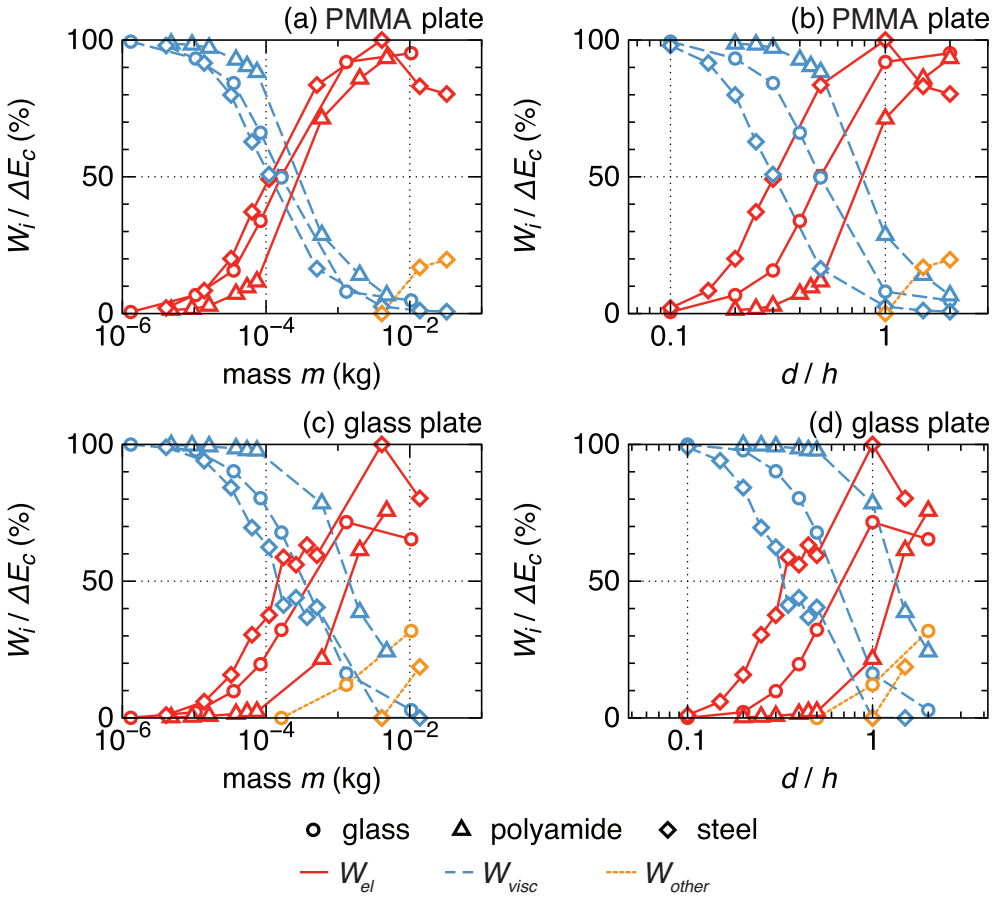

Figure 12. Percentage of the total energy lost in elastic waves $W_{el}/\Delta E_c$ (red full line), by viscoelastic dissipation $W_{visc}/\Delta E_c$ (blue dashed line) and by other processes $W_{other}/\Delta E_c$ (orange dotted line) as a function of (a)-(c) the bead mass m and (b)-(d) the ratio of the bead diameter d over the plate thickness h for impacts of glass (circles), polyamide (triangles) and steel (diamonds) beads dropped from height $H = 10$ cm on (a)-(b) the PMMA plate and on (c)-(d) the glass plate.

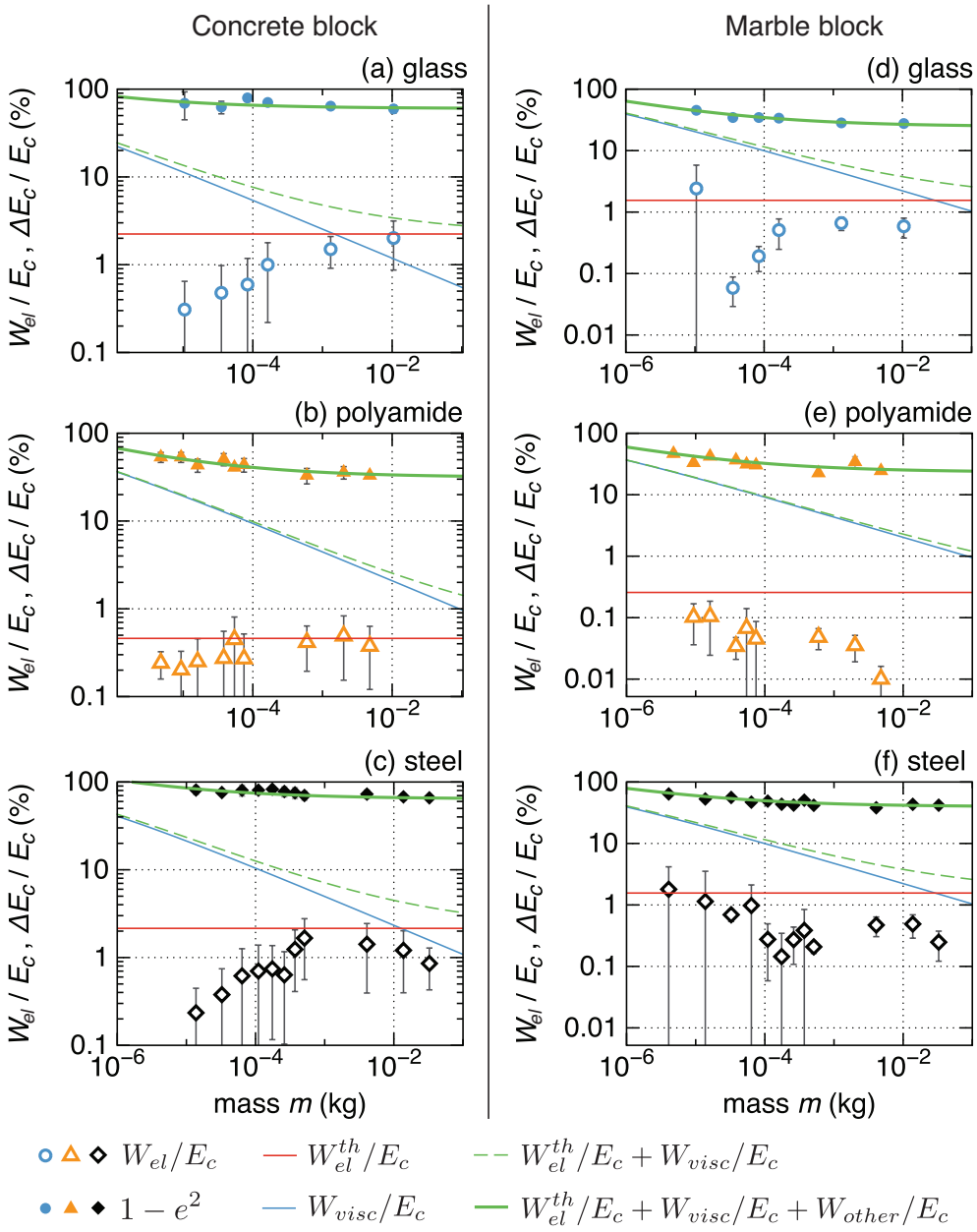

Figure 13. Ratio of the measured radiated elastic energy W_{el} over the impact energy $E_c = \frac{1}{2}mV_z^2$ (empty symbols) and measured lost energy ratio $\Delta E_c/E_c = 1 - e^2$ (full symbols) as a function of bead mass m for impacts of (a)-(d) glass, (b)-(e) polyamide and (c)-(f) steel beads on (a) to (c) the concrete block and on (d) to (f) the marble block. The red line represents the theoretical ratio W_{el}^{th}/E_c with W_{el}^{th} in equation (24) with $C_{block} = 0.02$. The blue line is the viscoelastic energy ratio W_{visc}/E_c [equation (35)]. The dashed green line is the theoretical lost energy ratio $W_{el}^{th}/E_c + W_{visc}/E_c$. The thick green line is the same ratio plus the percentage W_{other}/E_c of energy lost in other processes, which is assumed independent of the bead mass m (see text).

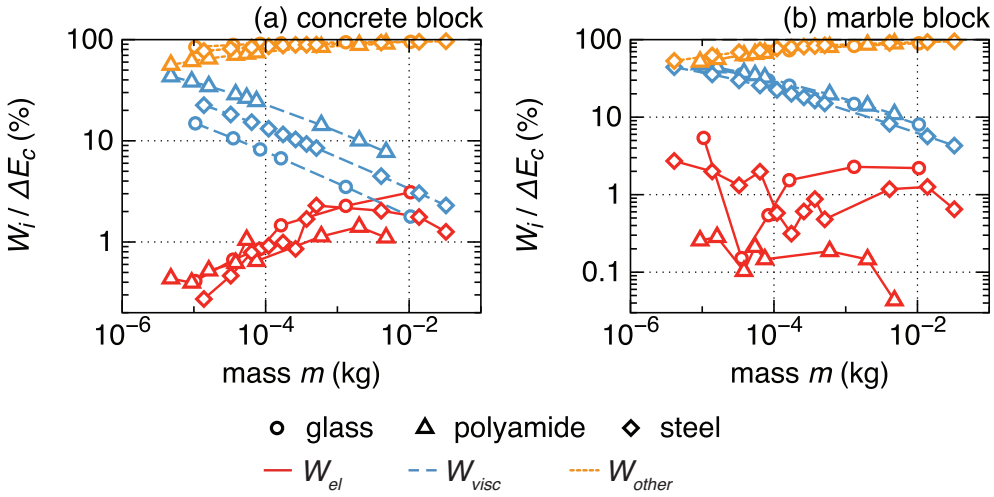

Figure 14. Percentage of the total energy lost in elastic waves $W_{el}/\Delta E_c$ (red full line), by viscoelastic dissipation $W_{visc}/\Delta E_c$ (blue dashed line) and by other processes $W_{other}/\Delta E_c$ (orange dotted line) as a function of the bead mass m for impacts of glass (circles), polyamide (triangles) and steel (diamonds) beads dropped from height $H = 10$ cm on (a) the concrete block and on (b) the marble block.

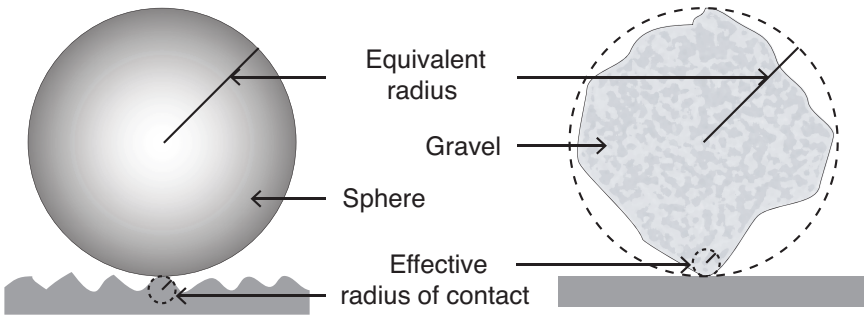

Figure 15. Schematic of the contacts between a sphere and a rough surface and between a rough gravel and a flat surface.

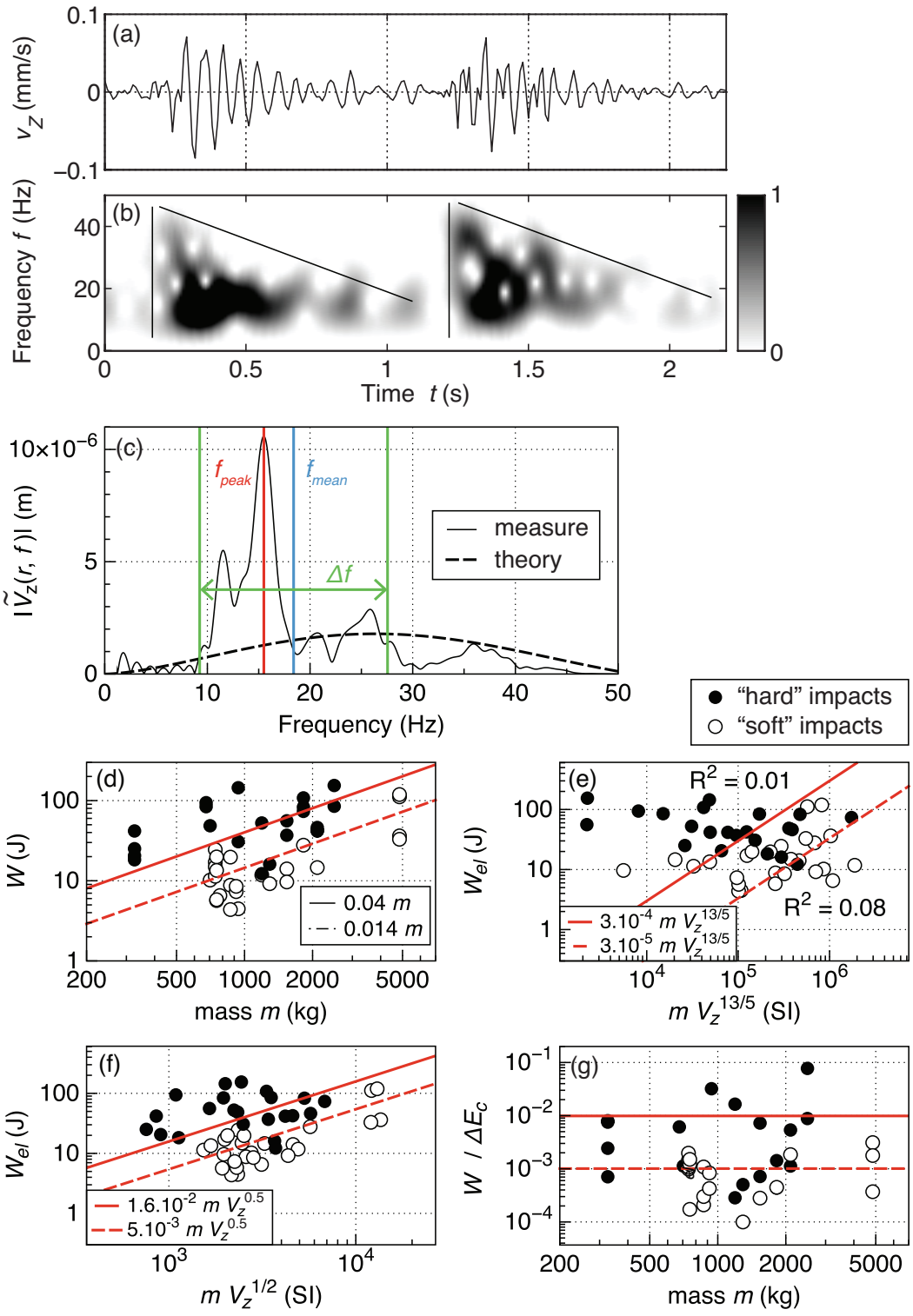

Figure 16. (a) Vertical vibration speed $v_z(r,t)$ generated by two successive impacts of a boulder of mass m = 326 kg on the rock slope. (b) Spectrogram of the signal in (a). Darker shape represents higher energy (normalized). The black lines highlight the triangular shape of the spectrograms. (c) Amplitude spectrum $|\tilde{V}_z(r,f)|$ for the first impact, with the peak f_{peak} and mean f_{mean} frequencies and the bandwidth Δf. Dashed line: synthetic spectrum computed with the convolution of *Hertz* [1882]'s force of elastic impact with the Green's function of Rayleigh waves. (d) to (f) Radiated elastic energy W_{el} for different boulders documented in Tahiti as a function of (d) the mass m and of parameters (e) $mV_z^{13/5}$ and (f) $mV_z^{0.5}$, with associated

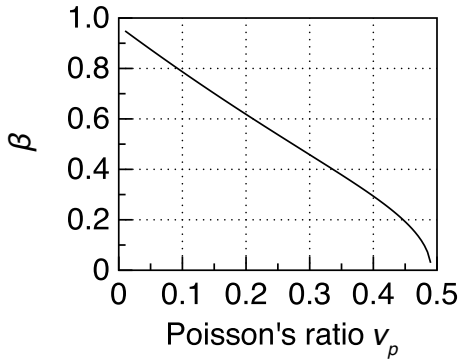

Figure 17. Coefficient β defined by equation (A7) as a function of the Poisson ratio ν_p.

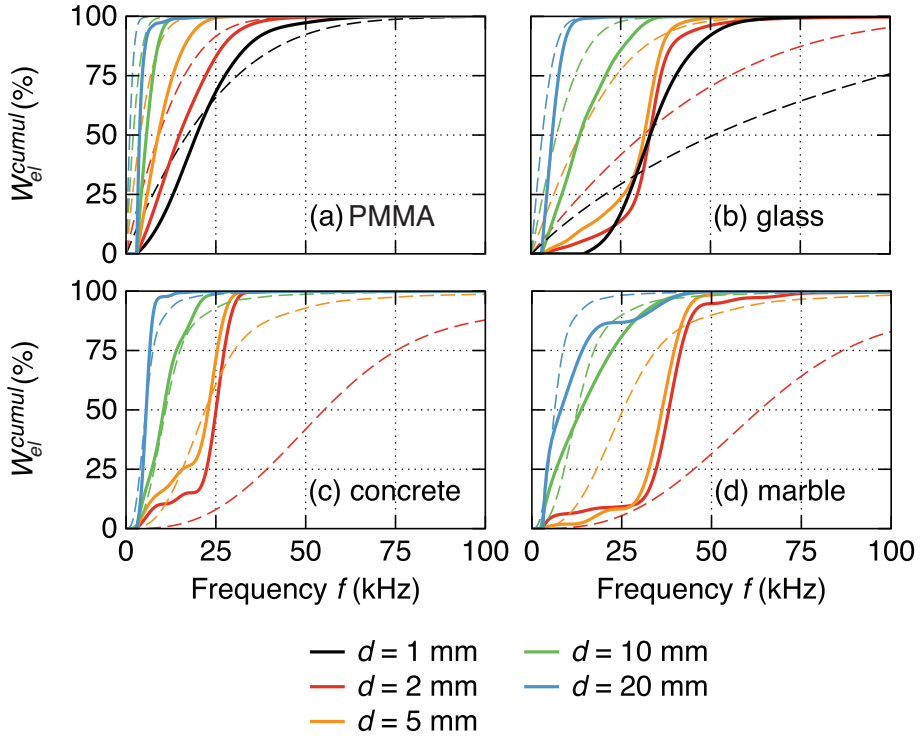

Figure 18. Cumulated radiated elastic energy W_{el}^{cumul} for the impact of steel beads of different diameters d (different colors) on (a) the PMMA plate, (b) the glass plate, (c) the concrete block and (d) the marble block, as a function of frequency f. Full line: experiments, dashed line: synthetics obtained with the convolution of the Green function with *Hertz* [1882]'s force of elastic impact.

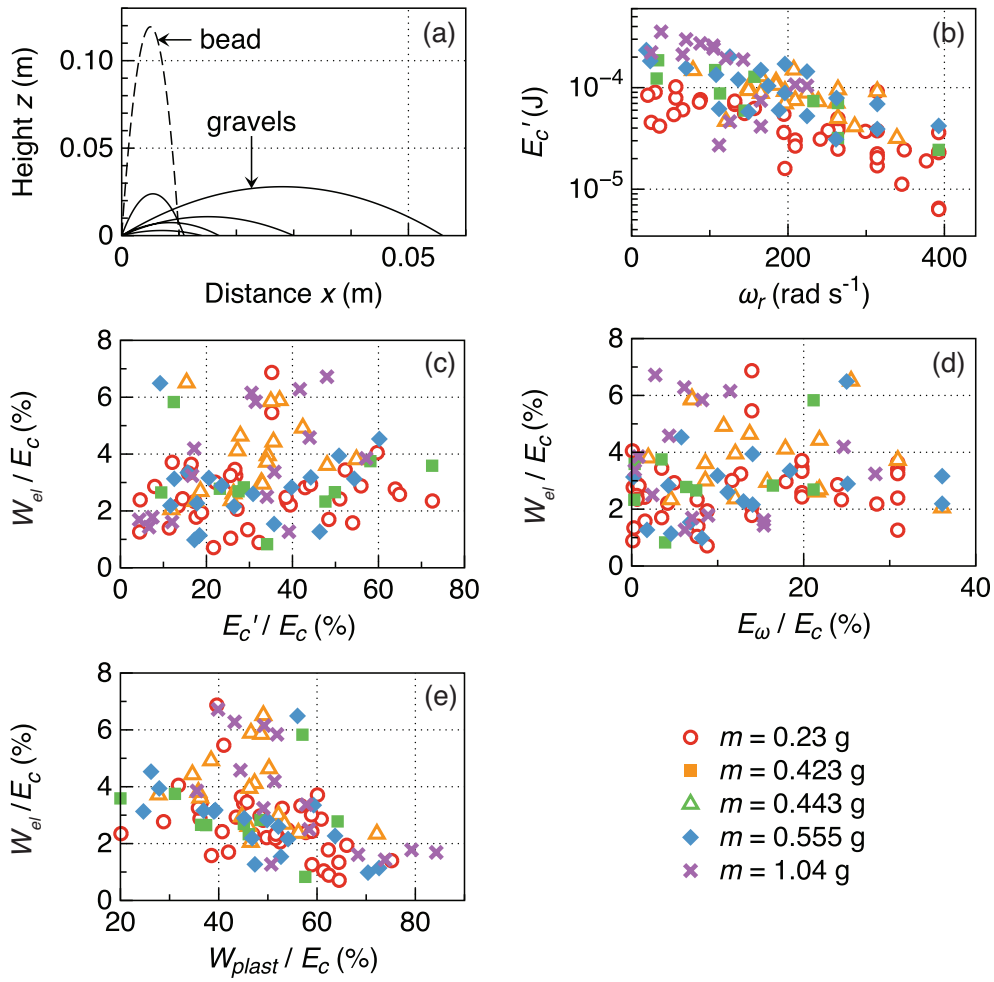

Figure 19. (a) Different rebound trajectories followed by the same gravel of mass $m = 0.23$ g dropped from height $H = 10$ cm several times on the glass plate (full lines) and one rebound trajectory followed a spherical bead of diameter $d = 4$ mm dropped from the same height H (dashed line). Gravels of different masses m (different symbols) are dropped without initial spin from height $H = 10$ cm on the glass plate. (b) Translational kinetic energy E_c' of the gravels after rebound as a function of their rotation speed ω_r after rebound. (c) to (e) Percentage of impact energy lost in elastic waves W_{el}/E_c as a function of the percentage of the impact energy E_c converted (c) in rebound translational energy E_c', (d) in rotational energy E_ω and (e) in plastic deformation W_{plast}.

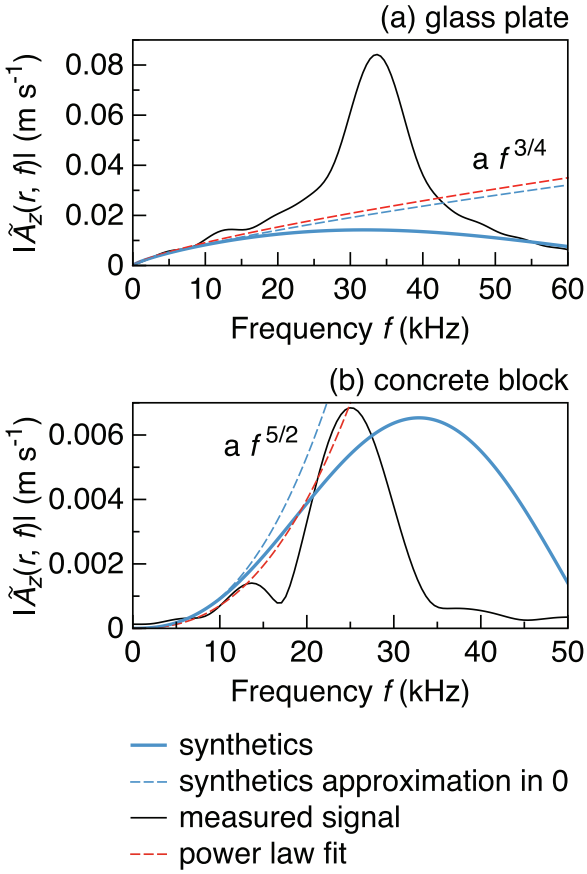

Figure 20. Measured amplitude spectrum $|\tilde{A}_z(r, f)|$ (black line) and synthetic spectrum (thick blue line) for the impact of a steel bead of diameter 5 mm on (a) the glass plate and (b) the concrete block. The blue dashed line is the power law approximation for low frequencies of the synthetic spectrum. The red dashed line is an adjustment of the low frequencies content of the measured spectrum with the power law.